Petroleum Science 23 (2026) 3988–4008

Contents lists available at ScienceDirect

Petroleum Science

journal homepage: www.keaipublishing.com/en/journals/petroleum-science

Original Paper

Magnetic coupling mechanism between high-intensity magnet and multiple close-range casings and casing positioning method: Numerical simulation and experimental study

Xu-Ping Ma [a], Zhong-Zhi Hu [a,*], Shao-Jie Fu [b], Yu-Dian Lei [b]

[a] *School of Mechanical Engineering, Sichuan University of Science & Engineering, Yibin, 644002, Sichuan, China*
[b] *PetroChina Company Limited, Jidong Oilfield Company, Tangshan, 063000, Hebei, China*

ARTICLE INFO

Article history:
Received 22 September 2025
Received in revised form
3 March 2026
Accepted 3 March 2026
Available online 5 March 2026

Edited by Jia-Jia Fei

Keywords:
Cluster well
Magnetic ranging
Anti-collision
Positioning
High-intensity magnet

ABSTRACT

In cluster wellbores, where casings are densely distributed with complex spatial relationships, drilling new wells poses a high risk of collision. To mitigate this, high-precision ranging and positioning technologies are essential. Existing magnetic ranging techniques have proven effective in applications such as cluster wells and relief wells. However, their limitations—including susceptibility to interference from adjacent wells, high operational costs, and poor adaptability to multi-casing environments—restrict their applicability in engineering practice. In this study, a method of ranging and positioning casing based on active excitation with a high-intensity magnet is proposed. The magnet and probe are both deployed within the drilling wellbore, thus preventing any disruption to adjacent well production while also allowing operation in complex environments with multiple closely-spaced casings. By magnetizing multiple close-range casings, this method exploits magnetic field coupling effects that inherently reflect casing quantity and distribution. A combination of spatial magnetic field coupling theory and numerical modeling was employed to analyze casing magnetization under coupled field, and sensitivity studies were carried out to evaluate factors influencing coupled field strength. The optimal sensor installation position relative to the high-intensity magnet was determined, and a continuous magnetic signal-based tubing positioning model was established. The geomagnetic component synchronized with the drill string's rotation frequency is extracted from the total magnetic field and used as a reference for the geomagnetic north. After geomagnetic filtering, a relative computational model for casing distance and azimuth was developed based on simulation results. A simulation experiment on the ground was further designed to validate the reliability of the numerical modeling. Results showed that the maximum absolute error in computed casing geomagnetic azimuth was 4.22°, while the maximum absolute error in distance was 0.08 m. This study not only introduces a new method but also provides an important theoretical foundation and data support for the advancement of magnetic ranging theory in complex downhole environments, as well as for subsequent inversion studies aimed at determining spatial positions from known magnetic field distributions.

1. Introduction

Cluster well technology has gained widespread application in offshore and onshore oilfield due to its ability to significantly conserve surface land use and efficiently develop oil and gas resources (Abramov, 2019; Liu et al., 2023). However, as cluster well platform densities continue to increase, wellbore collision prevention has become increasingly critical. Particularly in environments with dense well placement in upper vertical sections, the spatial localization of adjacent well casings and collision risk assessment have emerged as key technical bottlenecks constraining safe and efficient drilling operations (Liu et al., 2013; Hu et al., 2019).

* Corresponding author.
E-mail address: zhongzhi-hu@suse.edu.cn (Z.-Z. Hu).
Peer review under the responsibility of China University of Petroleum (Beijing).

https://doi.org/10.1016/j.petsci.2026.03.006
1995-8226/

Traditional methods for predicting well-to-well distance primarily rely on inclination data and trajectory scanning calculations, exhibiting cumulative errors that fail to meet the control requirements for high-precision collision avoidance during drilling (Ben et al., 2020; Williamson, 2000; Torkildsen et al., 2008; Dou et al., 2022; Cheng et al., 2023). Magnetic guidance distance measurement technology, by directly detecting magnetic signal sources from adjacent wells, avoids error propagation issues and has evolved into an indispensable high-precision guidance method for drilling complex structural wells (Gao and Diao, 2016; Hu et al., 2022). Based on magnetic source generation mechanisms, this technology is categorized into passive magnetic guidance and active magnetic guidance. Passive magnetic guidance utilizes residual magnetism in casing or geomagnetic field distortion effects. While offering the advantage of requiring no intervention from adjacent wells, it suffers from weak signals, susceptibility to environmental noise, and limited measurement accuracy (Lips et al., 2020; Zhang et al., 2020; Bahri et al., 2024). Active magnetic steering enhances detection signals by applying artificial magnetic field, achieving significant improvements in measurement range and accuracy (Jones et al., 1987; Duncan, 2013; Gao et al., 2013; Li et al., 2016; Yan et al., 2022; Dou et al., 2024; Qin et al., 2025). It has been successfully applied in high-risk operations such as rescue well drilling and re-entry into old wells (Dorey et al., 2021; Hao et al., 2021; Zhang et al., 2023; Li et al., 2024). Currently, most internationally developed active magnetic guidance systems, such as RMRS and MGT, still rely heavily on downhole or surface auxiliary equipment. This approach introduces challenges including high operational complexity, substantial costs, and potential interference with production wells (Poedjono et al., 2007; Poedjono et al., 2009; Wu et al., 2015; Dorey and Rassadkin, 2021).

In recent years, active magnetic guidance methods based on high-intensity magnets have demonstrated significant development potential. For instance, Dou et al. (2018) designed a rotating magnetic field ranging method based on a dual-magnet source structure, but it primarily applied to single-casing scenarios and featured a complex magnet configuration. Hu et al. (2023) proposed a method for detecting adjacent well casing by analyzing forces on high-intensity magnets, but its effective range was limited. Hu and Fu (2023) improved the mechanical model and experimentally validated its effectiveness near the drill bit, yet the detection distance remained restricted to 1 m. While these approaches eliminate the need for adjacent well operations, they fail to simultaneously address complex multi-casing scenarios and long-range detection requirements. In high-density cluster well drilling environments, multiple adjacent casings often coexist circumferentially during drilling, generating multi-source magnetic field coupling effects that significantly increase signal complexity. This poses severe challenges for existing methods in casing quantity identification and precise localization.

To address the technical challenge of precise multi-casing localization in complex magnetic environments, this paper proposes a novel theoretical method for adjacent well casing localization based on the magnetization mechanism of rotating high-intensity magnets and dynamic magnetic field coupling. The theoretical innovation lies in systematically elucidating the magnetization mechanism of multiple casings under rotating high-intensity magnet excitation, the principle of extracting the geomagnetic reference direction, and the inversion model for multi-source coupled magnetic field. This establishes a comprehensive theoretical framework for simultaneously solving the distance and azimuth of multiple casings from composite dynamic magnetic field signals. By integrating rotating high-intensity magnets into the drill string assembly to excite adjacent casings and generate induced magnetic field, and utilizing a triaxial magnetometer to collect dynamic magnetic field signals, the method achieves precise determination of the absolute orientation of casings by analyzing signal components related to the geomagnetic field direction reference. Compared to traditional methods reliant on magnetic tool face, this approach generates alternating magnetic field via rotating high-intensity magnet and leverages the coupling effect between the geomagnetic field and dynamic rotating magnetic field to accurately indicate geomagnetic north. Leveraging the stability of the geomagnetic direction, this method extracts magnetic north signals from dynamically coupled magnetic field. It effectively mitigates numerical interference caused by fluctuations in geomagnetic field strength and magnetization from multiple casings, resolving the challenge of directional positioning in multi-casing environments (ElGizawy et al., 2022, 2024). This provides a novel theoretical foundation and technical approach for collision-avoidance drilling in cluster wells. This study systematically analyzes magnetic field distribution patterns and dynamic response characteristics in multiple close-range casings environments by establishing a multiphysics coupling numerical model. The method's effectiveness and engineering applicability were validated through full-scale ground experiments. These findings hold significant theoretical and practical value for enhancing cluster well drilling safety and advancing magnetic guidance and distance measurement technology.

2. Theory and methodology

2.1. Positioning principle

Fig. 1 illustrates the principle of locating multiple closely spaced casings using an alternating magnetic field. A high-intensity magnet rotating about a fixed axis generates a spatially alternating magnetic field. The casings, with relatively high magnetic permeability, become magnetized and produce secondary magnetic field that, together with the source magnetic field and the geomagnetic field, form a spatially coupled magnetic field. By monitoring the time-varying magnetic field at a specific point along rotation axis of the magnet, a characteristic time-series curve of the coupled magnetic field can be established. The relationship between this curve and the complex spatial distribution of multiple casings enables accurate azimuthal positioning of the casings.

As shown in Fig. 2(a), the magnetic field strength of the magnetic source is represented by a series of radial vectors along the horizontal circle defined by the magnet's north–south poles. The geomagnetic field is simplified as a planar field perpendicular to the casing, with the geomagnetic field strength denoted as $\boldsymbol{B}_{\mathrm{g}}$, the rotating magnet's field as $\boldsymbol{B}_{\mathrm{s}}$, and the superimposed field as $\boldsymbol{B}_{\mathrm{o}}$. According to the principle of magnetic field superposition, $\boldsymbol{B}_{\mathrm{o}}$ is an alternating magnetic field. By analyzing the field strength variation at an observation point above the magnet and the geomagnetic deflection angle β, the geomagnetic north direction can be determined. During the rotation of the magnetic source, adjacent casings are magnetized by the alternating field, producing a casing-induced magnetic field $\boldsymbol{B}_{\mathrm{c}}$, which couples with the superimposed field $\boldsymbol{B}_{\mathrm{o}}$ to form a resultant field $\boldsymbol{B}$, as illustrated in Fig. 2(b). By investigating the coupling characteristics between the alternating field and the casing-induced field, the geomagnetic azimuth of adjacent casings can be accurately established.

2.2. Spatial magnetic field coupling calculation

2.2.1. Magnetic dipole model

In actual drilling operations, the bottom-hole assembly (BHA) rotates dynamically with the drill bit, making it unsuitable to

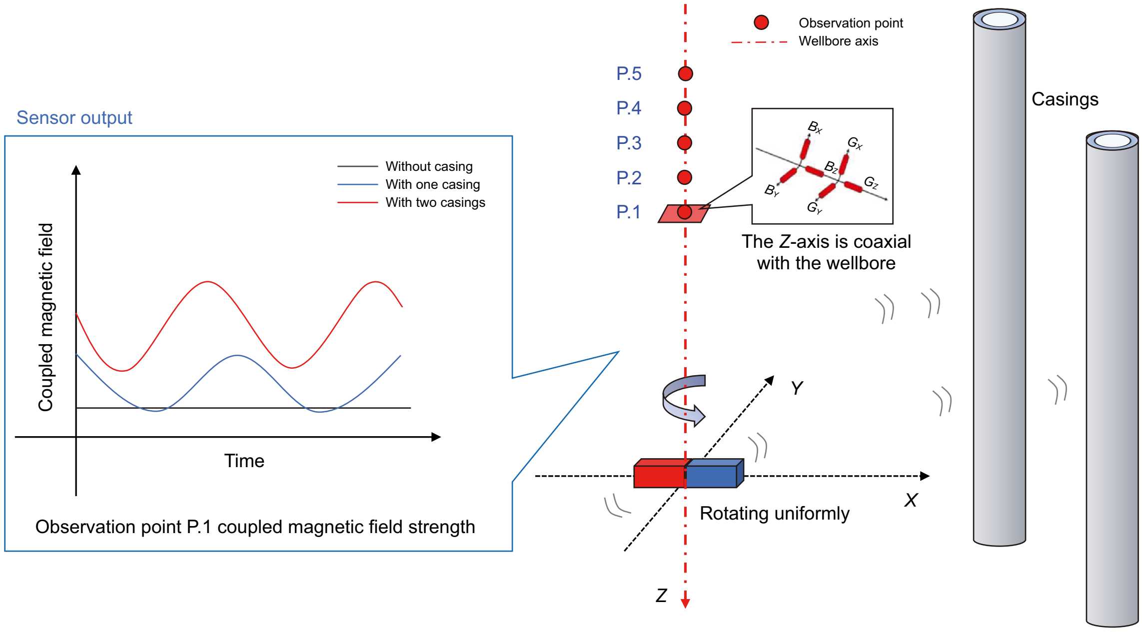

Fig. 1. Schematic diagram of multiple close-range casings positioning in alternating magnetic field.

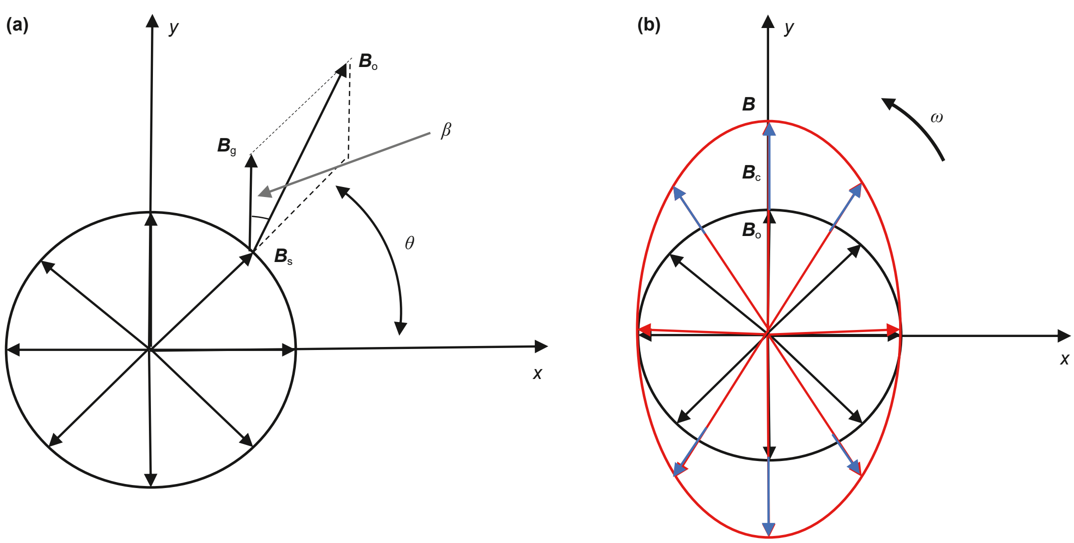

Fig. 2. Vector diagram: (**a**) Geomagnetic field deflection and (**b**) magnetic field coupling.

directly apply a static magnetic dipole model for target localization (Zong et al., 2011). The magnetic field of a rotating dipole resembles that of a static dipole, but the dipole moment of the former varies periodically in direction. When a magnetic source is placed near the bit and rotates together with it, a dynamic rotating dipole system is formed, as illustrated in Fig. 3. A Cartesian coordinate system is established using the three orthogonal axes of the triaxial magnetic field sensor, where the z-axis aligns with the axis of the downhole drilling tool. It is assumed that the dipole moment initially points in the negative y-axis direction, and then the dipole begins rotating counterclockwise about the z-axis. At a given time step k during rotation, the equivalent dipole moment is $\boldsymbol{m}_k$, with its projection in the xoy plane forming an angle α_k relative to the negative y-axis. The magnetic field strength $\boldsymbol{B}$ of the dipole at a spatial point $P\,(x, y, z)$ can then be expressed as follows:

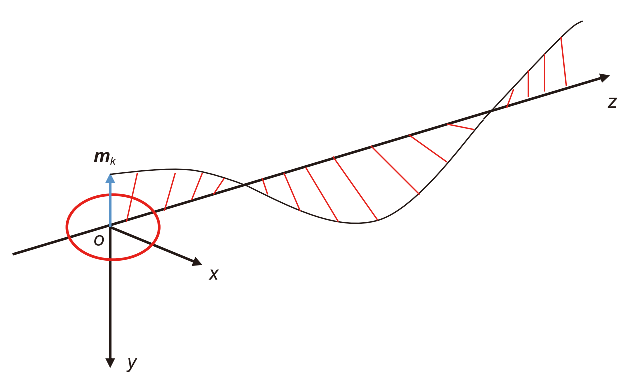

Fig. 3. Schematic diagram of rotating magnetic dipole.

$$\boldsymbol{m}_k = (0,\ \boldsymbol{m}_k \sin(\alpha_k),\ \boldsymbol{m}_k \cos(\alpha_k)) \tag{1}$$

$$\boldsymbol{B}(\mu_0, r) = \frac{\mu_0}{4\pi}\left[\frac{3(\boldsymbol{m}_k \cdot r)r}{r^5} - \frac{\boldsymbol{m}_k}{r^3}\right] \tag{2}$$

In Eq. (2), where μ_0 is the vacuum permeability, and r is the distance from the magnetic source to spatial point P.

In magnetic dipole theory, the point dipole assumption provides sufficient accuracy in the far-field region, but introduces significant errors in the near-field range due to the finite-size effects of the magnet. To quantify this error, an error estimation model based on magnetic multipole expansion theory can be established, with the ratio of the characteristic size to the observation distance as the key variable.

$$\varepsilon(r) = \left(\frac{L}{r}\right)^2 \times K \tag{3}$$

In Eq. (3), where L is the characteristic dimension of the magnetic source (in this study, the height of the permanent magnet is 100 mm), and K is a constant related to the geometric shape of the magnetic source (for a cylindrical magnet, $K = 0.3$). This error model has been demonstrated and applied in the error analysis of magnetic dipole approximations (Jackson, 2021). According to estimations based on this model, when the observation distance exceeds 0.5 m, the theoretical relative error can be controlled within 2%, indicating that the magnetic dipole model maintains good applicability within this range and is suitable for the near-field coupling analysis of interest in this study.

It should be specifically noted that this study aims to address the engineering positioning of collision avoidance for casing in cluster wells. In this application scenario, due to safety drilling requirements, the collision avoidance safety distance is typically restricted to 1 m or greater. Accordingly, all analyses and modeling are conducted for safety detection distances of 1 m and above. Near-field conditions beyond this range are excluded from consideration as they involve actual avoidance maneuvers. This defined scope enables the application of the magnetic dipole model within its precise far-field region, inherently avoiding near-field errors while ensuring both theoretical validity and engineering applicability of the methodology.

2.2.2. Volume element partitioning

Assume that ΔV_i is a volumetric element segmented from the casing. Each element is further divided into many small regions, and its magnetic moment after magnetization is denoted as $m_{\Delta V_i}$. Since ΔV_i is very small and located relatively far from the sensor, it can be approximated as a magnetic dipole. After calculating each $m_{\Delta V_i}$, the total magnetic moment of the casing can be obtained by superimposing all such dipoles. In this study, the minimum horizontal distance between the casing and drill pipe is 1 m. Due to constraints in applying magnetic dipole theory (the distance-to-element-size ratio must exceed 15), volume element ΔV_i is approximated as a cube with a maximum edge length of 0.2 mm. This yields a minimum distance-to-element-size ratio of 150, satisfying the requirements for applying magnetic dipole theory.

Fig. 4 illustrates the principle of discretizing the casing into volumetric elements ΔV_i. First, the annular space along the axial direction is divided with a fixed step size δ. Then, in the radial direction, concentric sub-annular regions are generated from the inner radius R_a to the outer radius R_b with step size δ. Finally, the circumferential direction is partitioned into equal arc segments, forming a structured hexahedral mesh of volumetric elements.

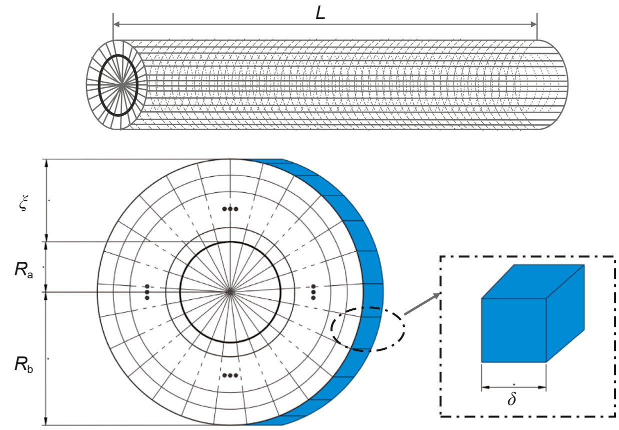

Fig. 4. Schematic diagram of microelement volume partitioning.

Here, L denotes the casing length, ξ the casing thickness, R_a the inner radius, R_b the outer radius, and δ the segmentation step size.

2.2.3. Magnetic field strength calculation

The magnetic field measured by the sensor consists of three components: the magnetic field from the source, the geomagnetic field, and the magnetization field of adjacent casings. Among these, the field generated by the high-intensity magnet is the dominant contributor to casing magnetization. The magnetic sensor is positioned at a vertical distance S(m) above the high-intensity magnet. According to Eq. (1), the source magnetic field $\boldsymbol{B}_s$ measured by the sensor can be expressed as:

$$\boldsymbol{B}_s(\mu_0, z) = \frac{\mu_0}{4\pi}\left[\frac{3(\boldsymbol{m}_k \cdot z)z}{z^5} - \frac{\boldsymbol{m}_k}{z^3}\right] \tag{4}$$

Assuming the ferromagnetic material of the casing is isotropic, during drilling the casing becomes uniformly magnetized with no residual magnetism considered. The permeability and magnetic susceptibility of the casing are μ_1 and χ_m, respectively. The magnetic moment ΔV_i is given by the following equation:

$$m_{\Delta v_i} = \frac{\Delta V_i \cdot \chi_m \cdot B_i}{\mu_1} \tag{5}$$

When the microelement ΔV_i on the casing is magnetized, it generates a magnetic flux density B_i at the magnetic field sensor. Given the formation's magnetic permeability is μ, the magnetized magnetic field B_i generated by the microelement ΔV_i on the casing at point S can be determined.

$$B_i = \frac{\mu_0}{4\pi}\left[\frac{3(m_{\Delta V_i} \cdot r)r}{r^5} - \frac{m_{\Delta V_i}}{r^3}\right] \tag{6}$$

From the above formula, the magnetizing field at the magnetic field sensor for any ΔV_i on the casing can be obtained. This paper assumes the casing is infinitely long and isotropic, meaning any point on the casing will be magnetized. The magnetizing field at point S is the sum of all ΔV_i magnetizing field at the sensor.

$$\boldsymbol{B}_c = \sum B_i \tag{7}$$

The magnitude of the geomagnetic field is obtained through measuring instruments and denoted as $\boldsymbol{B}_g$. The magnetic flux density $\boldsymbol{B}$ detected by the magnetic field sensor is:

$$\boldsymbol{B} = \boldsymbol{B}_c + \boldsymbol{B}_s + \boldsymbol{B}_g \tag{8}$$

3. Research plan

This paper employs COMSOL Multiphysics and its “Magnetic Field, No Current” physics interface for model development and numerical analysis. Leveraging its multiphysics coupling capabilities, it accurately simulates the complex electromagnetic phenomena involving alternating magnetic field and magnetization coupling across multiple tubes. The analysis disregards the influence of free currents, making it suitable for the scenario without external current excitation described herein. By employing the magnetic flux conservation Eq. (9) from Maxwell's equations, the magnetic flux density distribution within the space is calculated. This enables analysis of the magnetic field characteristics generated by the magnetic source at different spatial locations.

$$\begin{cases} \nabla \cdot \boldsymbol{B} = 0; \\ \nabla \times \boldsymbol{H} = 0; \\ \boldsymbol{H} = -\nabla V_{\mathrm{m}} \end{cases} \tag{9}$$

Assuming the casing material is a linear, isotropic ferromagnetic material, the relative permeability of the casing is a constant, with

$$\boldsymbol{B} = \mu \boldsymbol{H} \tag{10}$$

Ferromagnetic materials exhibit the characteristic of easy magnetization. Their magnetization intensity M is directly proportional to the magnetic field strength $\boldsymbol{H}$ generated by a high-intensity magnet, expressed as

$$M = \chi_{\mathrm{m}} \boldsymbol{H} \tag{11}$$

In Eq. (12), μ is the magnetic susceptibility of the casing, a dimensionless constant. The relative magnetic permeability μ_{r} is the ratio of the magnetic permeability of the magnetic medium to that of free space μ_0, representing a magnetic property that characterizes the magnetism and ease of magnetization of a material, expressed as

$$\mu_{\mathrm{r}} = \frac{\mu}{\mu_0} \tag{12}$$

3.1. Numerical simulation solution

This study establishes a numerical model based on the actual wellbore dimensions of cluster wells, utilizing the magnetic field curve characteristics measured by triaxial magnetometers as the core criterion for casing orientation and distance inversion.

First, due to variations in geomagnetic field parameters across the actual drilling area, this study temporarily disregards geomagnetic effects. The focus is on analyzing the magnetization effects of alternating magnetic field on casing and the disturbance responses they induce within the spatial magnetic field. This phase aims to preliminarily clarify the fundamental coupling mechanism between the magnetic source and casing, establishing a magnetic field interaction model under conditions free from geomagnetic interference. Building upon this foundation, a sensitivity analysis employing single-factor methods is conducted on multiple key parameters—observation point location, casing distance, and casing count—to evaluate their influence on the intensity of the spatially coupled magnetic field and its variation patterns. This provides guidance for mapping the relationship between different spatial distributions of casing and the characteristic curves of the spatially coupled magnetic field. The baseline values for each parameter are listed in Table 1. Subsequently, a magnetic source-casing coupling field model under geomagnetic conditions was established. Continuous magnetic signals were interpreted to determine the geomagnetic north direction, filtering the geomagnetically restored magnetic source-casing coupling field to lay the foundation for precise casing localization. The model assumes a geomagnetic field strength of 40 μT, with the magnetic north direction oriented at 45° in the coordinate system.

Finally, based on the revealed magnetic source-casing coupling mechanism, sensor placement positions were determined, and a casing positioning inversion model was constructed, providing theoretical basis and parameter guidance for subsequent experiments.

It is worth noting that due to the complexity of multi-casing spatial distribution, the multi-casing model established in this paper only discusses single-casing and dual-casing scenarios, with the dual-casing axes maintaining equal horizontal distance from the magnetic source axis. The observation point height is defined as the distance between the high-intensity magnet and the sensor measurement point. As shown in Fig. 5, the casing positioning line is marked with a red dashed line. Positioning angle (θ) is defined as the angle between the x-axis and the positioning line, inter-casings angle (α) is the angle formed by the line connecting the centers of the two casings and the origin, and casing distance (d) is the horizontal distance between the casing and the magnet. In the subsequent analysis, the rotation angle of the high-intensity magnet matches the angle shown in Fig. 5.

Table 1
Parameter baseline values.

Parameters	Value
Casing height H_{c}, mm	2.0×10^4
Casing number n	1
Casing distance d, mm	1000
Positioning angle θ, °	0
Inter-casings angle α, °	0
Observation point height H_{p}, mm	2000

3.2. Finite element modeling

In the numerical simulation model, the magnetic source employs a cylindrical high-intensity magnet. A three-axis coordinate system is established with the magnet's center of mass as its origin. The magnet rotates about this origin within the X-Y plane, with its axis initially parallel to the x-axis. The computational domain is a sphere with a radius of 10 m, where the casing axis is parallel to the z-axis. To accurately simulate actual operating conditions, infinite element domains are set at the model boundaries. Geometric parameters are determined based on the actual wellbore and casing dimensions, as listed in Table 2.

3.3. Grid setup and irrelevance analysis

The numerical simulation model in this paper employs a spherical computational domain with a radius of 20 m, containing small-sized high-intensity magnets and a relatively large-diameter casing. To enhance the accuracy and stability of computational results while reducing computational load, the mesh generation strategy adopts the following approach: Mapping meshes are applied to the high-intensity magnets and casing, with cell aspect ratios maintained below 12. Mesh refinement is implemented near the casing and magnet regions to ensure critical area mesh quality. Mesh density gradually decreases outward to reduce computational effort. The mesh gradually becomes sparser outward to reduce computational load. The domain is subdivided into six mesh refinement levels from coarse to fine. Using the 5 m point along the z-axis as the

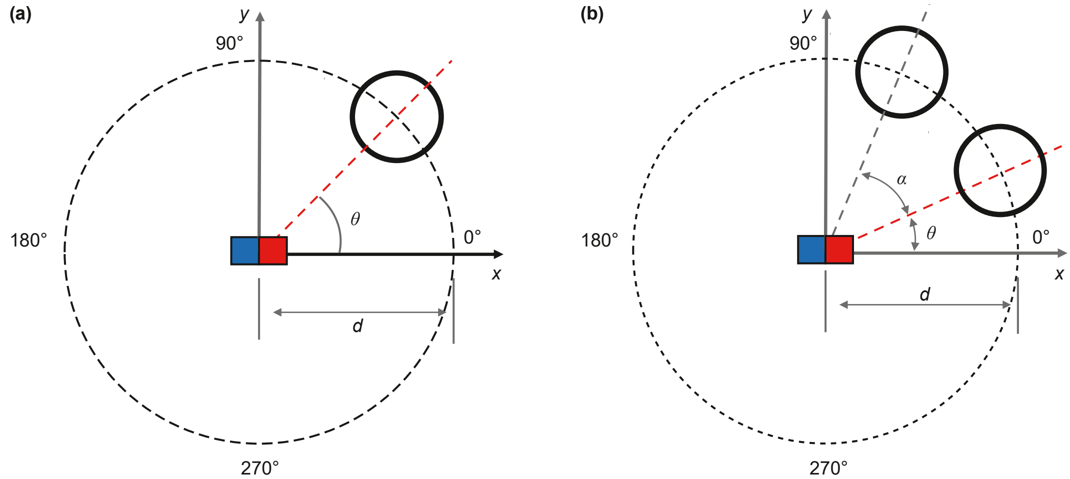

Fig. 5. Schematic diagram of casing distribution plan.

Table 2
General parameters for numerical simulation.

Object	Parameters	Value
Casing	Diameter, mm	244.5
	Thickness, mm	10
	Relative permeability	4000
High-intensity magnet	Length, mm	100
	Diameter, mm	80
	Rotation rate, Hz	1
	Magnetization, A/m	1.2×10^6
Air model	Diameter, mm	2.0×10^4
	Relative permeability, N/A^2	$4\pi \times 10^{-7}$

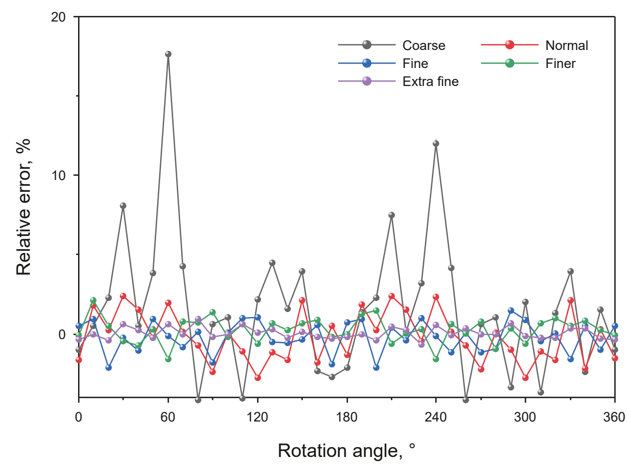

Fig. 7. Grid-independent verification.

observation point, the stability of the magnetic field strength along the *z*-axis is employed as the metric for evaluating mesh independence. The extremely fine mesh is selected as the baseline for determining the mesh partitioning scheme, with relative errors for other mesh levels shown in Fig. 7. Fig. 7 shows that the average relative errors of the coarse, normal, fine, finer, and extra fine meshes relative to the finest mesh are 1.65%, −0.18%, −0.18%, 0.14%, and 0.05%, respectively. Among these, the extra fine grid exhibits the smallest average relative error (0.05%), closely matching the extremely fine grid, with a maximum relative error of 0.92%. Balancing computational accuracy and efficiency, the extra fine grid was selected for subsequent calculations. Detailed grid partitioning is illustrated in Fig. 6.

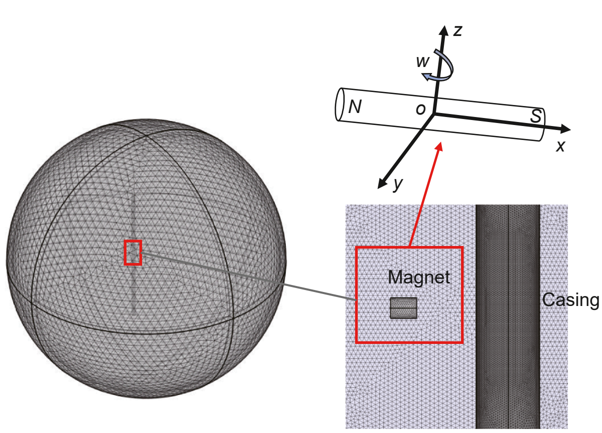

Fig. 6. Model mesh diagram.

3.4. Basic assumptions

In the magnetic measurement methods employed in this study, we established a fundamental assumption: the target strata do not contain strongly ferromagnetic minerals (such as magnetite). This is because such minerals induce intense geomagnetic interference, causing severe distortion of magnetic field signals and rendering magnetic-based positioning methods ineffective (Eatough et al., 2018; Hu et al., 2021). All models and conclusions in this study are based on the premise of non-ferromagnetic strata.

Since the geomagnetic field can be considered constant at the spatial observation point, and the induced magnetic field generated by the geomagnetically magnetized casing acts within a range of 0.5 m around the casing (Zhang et al., 2015), the casing detection range is set to 1 m or beyond. At the observation point, the magnetization field of the casing induced by the geomagnetic field is disregarded.

Additionally, it is assumed that the high-intensity magnet is an anisotropic material, while the casing is isotropic with zero

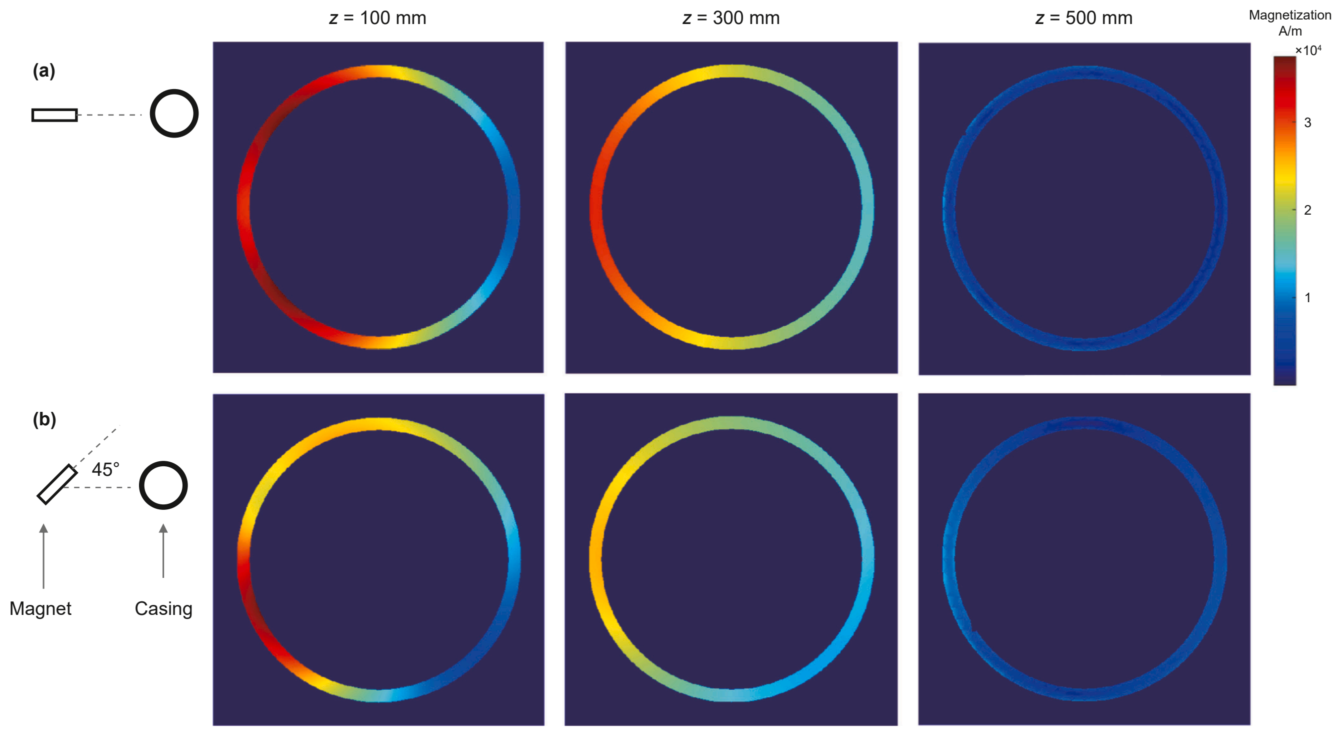

Fig. 8. Horizontal magnetization cloud map.

coercivity. The casing is uniformly magnetized in the magnetic field, and its inherent remanence is disregarded.

4. Results analysis

4.1. Magnetization effect of the casing

Fig. 8 illustrates the horizontal magnetization distribution of the casing under two conditions: (a) when the axis of the high-intensity magnet is aligned with the casing axis, and (b) when it is inclined at a 45° angle. Multiple horizontal cross-sections at different vertical distance (z) along the casing axis are selected for comparison. In both cases, the casing exhibits pronounced magnetization characteristics, with the direction of maximum to minimum surface magnetization strength aligned with the axis of the magnetic source. The maximum magnetization intensity reaches up to 3.75×10^4 A/m. By comparing Fig. 8(a) and (b), it can be observed that the magnetization intensity is significantly higher when the high-intensity magnet is directly aligned with the casing axis than when an angular offset exists. This indicates that the magnetization effect is more pronounced when the magnetic pole directly faces the casing. Moreover, the magnetization on the side of the casing closer to the magnet is consistently stronger than that on the far side, and the overall magnetization intensity gradually decays with increasing vertical distance. These results demonstrate that under magnetic source excitation, the induced magnetization field distribution within the casing closely follows the external magnetic field distribution. The side of the casing near the N pole of the magnet behaves as an N pole, reflecting a typical pole-induced response characteristic.

Fig. 9 presents the vertical magnetization intensity distribution of the casing. As shown, the magnetization intensity exhibits an up–down symmetric pattern with respect to the plane containing the axis of the magnetic source, and the magnetization directions on the two sides are opposite. The right half of the casing shows significantly lower magnetization intensity compared with the left half. Along the casing axis, the magnetization intensity first increases from the middle region to reach a peak, and then gradually decreases toward the ends. The axial magnetization intensity curves at different heights indicate that the distribution pattern remains consistent, with the maximum intensity occurring at approximately ±200 mm along the y-axis. Taking 200 mm as a reference, the maximum absolute deviation is 20 mm, and the variation ratio is less than 0.4%, which can be considered negligible. For a 1 m casing, the peak magnetization intensity is 3.7×10^4 A/m, while for a 10 m casing, the peak value increases to 4.7×10^4 A/m. This phenomenon demonstrates that casing height affects only the magnitude of magnetization intensity but does not alter its distribution pattern. Therefore, the magnetic field coupling mechanism analyzed using the 10 m casing is applicable to actual drilling conditions. In subsequent experiments, where the casing height is limited to less than 10 m, it is sufficient to adjust the casing height in the simulation to match the experimental conditions, ensuring the validity of the casing localization model.

4.2. Analysis of spatial magnetic field interference caused by casing magnetization

The time-varying magnetic field excited by a rotating high-intensity magnet induces magnetization within high-permeability metal casings. The coupling between this induced magnetization field and the source magnetic field leads to a distinctive spatial magnetic field distribution, which can serve as an effective indicator for casing azimuth identification. Fig. 10 illustrates the evolution of the coupled magnetic field under alternating-field magnetization of multiple casings, as well as the influence of casing number on the temporal magnetic field characteristics.

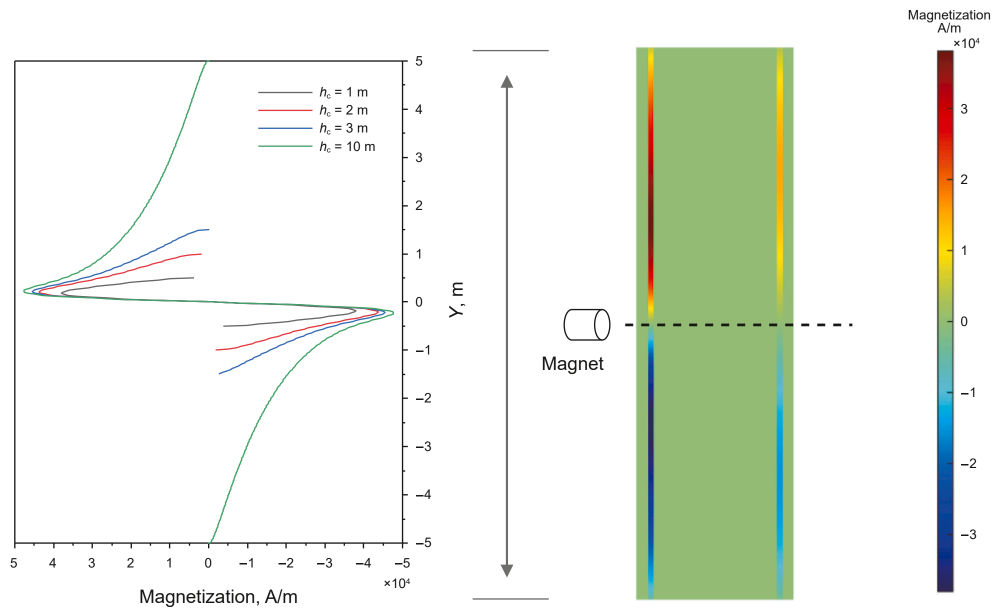

Fig. 9. Vertically magnetized cloud map.

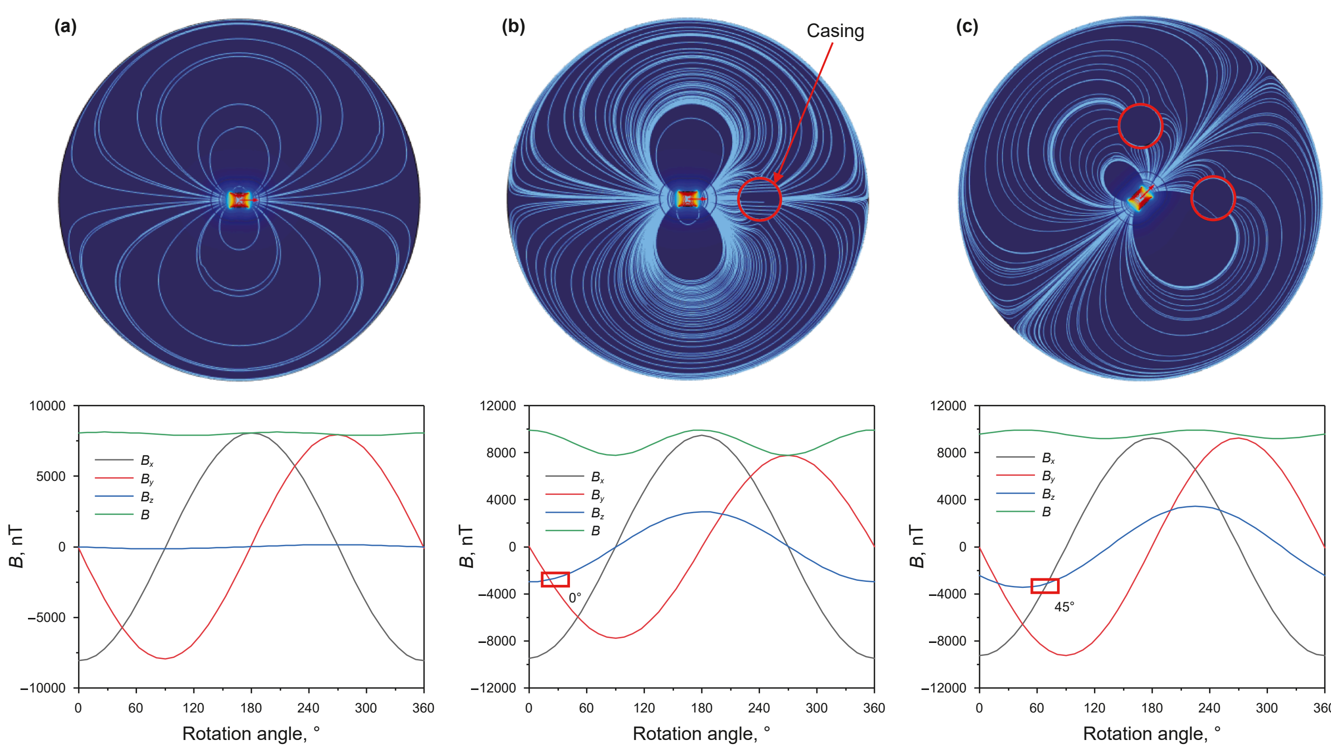

Fig. 10. Coupled magnetic field evolution and corresponding time-domain curves: (**a**) without casing, (**b**) one casing, (**c**) two casings.

When casings are present around the drilling well, compared with the no-casing scenario, the magnetic induction lines of the coupled field concentrate around the casings. This concentration causes significant disturbances in the time-varying curves of the three-axis magnetic induction intensity, and the overall field strength is notably enhanced. In Fig. 10(a), representing the no-casing condition, the *z*-axis magnetic field remains constant with zero amplitude. In Fig. 10(b), when the north pole of the magnet is oriented toward the casing axis center (0° azimuth), the *z*-axis magnetic field exhibits the maximum negative disturbance. In Fig. 10(c), with two casings distributed at a 90° angle, the *z*-axis likewise records the maximum negative magnetic signal when the north pole of the magnet points to the midpoint between the two casings (45° azimuth).

These observations clearly demonstrate that the presence of casings introduces identifiable disturbances into the time-varying magnetic field curves, with distinct azimuthal and spatial distribution characteristics. This finding preliminarily reveals the

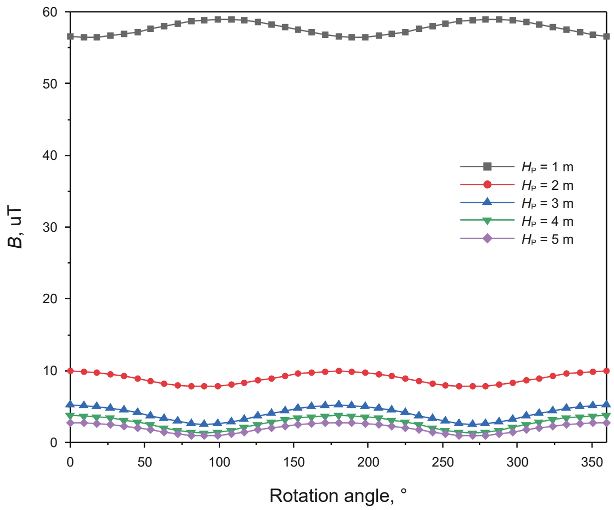

Fig. 11. Variation of magnetic field strength at observation points with rotation angle.

magnetic coupling mechanism between multiple casings and a rotating magnetic source, thereby providing a theoretical basis for casing localization based on magnetic field features.

4.3. Analysis of the magnetic field mechanism in magnet-casing coupling

4.3.1. Observation point height

The relationship between the coupled magnetic field strength at different observation points and the rotation angle of the high-intensity magnet is shown in Fig. 11. As shown in Fig. 11, the measured spatial magnetic field signal exhibits a distinct sinusoidal variation pattern. Its intensity gradually attenuates with increasing height at the observation point, and the amplitude decay follows an exponential function characteristic. When H_p is 1 m, the coupled magnetic field strength exhibits a sinusoidal pattern that first increases and then decreases. At distance of 2, 3, 4, and 5 m, the magnetic field strength shows a sinusoidal variation that first decreases and then increases, with the phase opposite to that at 1 m. This phenomenon indicates that the observation point location significantly influences the phase distribution of the coupled magnetic field. This pattern provides crucial guidance for optimizing the sensor installation location in subsequent stages.

4.3.2. Casing distance

Fig. 12(a) presents the variation of the time-domain coupled magnetic field strength with the rotation angle of the high-intensity magnet under different casing distance as well as the no-casing condition. Taking the peak value of the magnetic field strength curve in the no-casing scenario as the reference, Fig. 12(b) further illustrates the relationship between the difference in peak magnetic field strength and casing distance.

As shown in Fig. 12(a), the peak value of the time-domain coupled magnetic field strength curve decreases sharply with increasing casing distance. At a distance of 1 m, the peak value of the magnetic source-casing coupled magnetic field strength is significantly higher than in other operating conditions; whereas at a distance of 6 m, its peak value approaches the response level under no-casing conditions. As shown in Fig. 12(b), at a casing distance of 6 m, the difference between the peak coupled magnetic

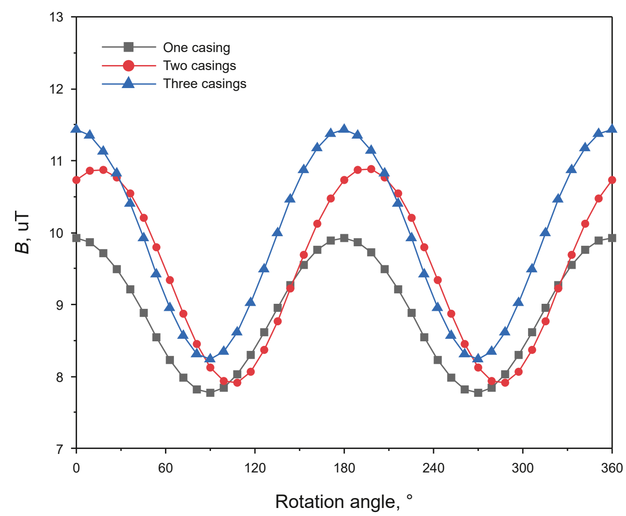

Fig. 13. Variation of magnetic field strength with rotation angle for different numbers of casings.

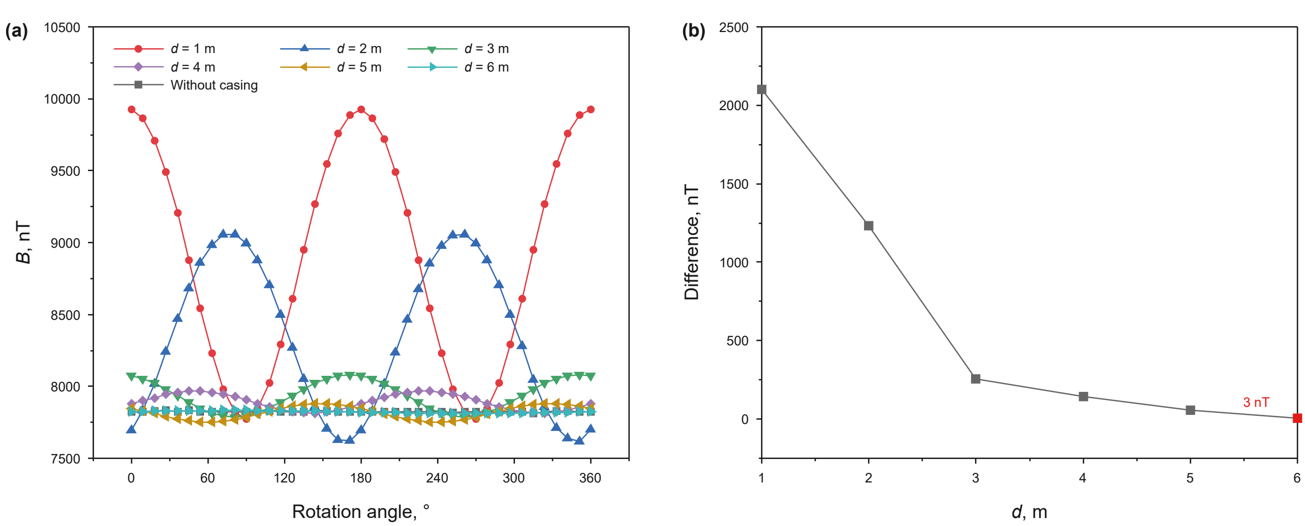

Fig. 12. Variation of magnetic field with different casing distance: (**a**) magnetic field strength curves and (**b**) peak difference relative to the no-casing condition.

field and the no-casing condition is only 3 nT. Considering the measurement accuracy of the triaxial magnetometer used is 1 nT, this signal strength is approaching the detection limit. This result indicates that within the accuracy range of the existing instrument, the effective magnetization range of the casing by the alternating magnetic field generated by the rotating high-intensity magnet does not exceed 6 m. Therefore, the effective detection distance for the magnetic source-magnetized casing coupling mechanism can be determined to be a maximum of 6 m.

4.3.3. Casing number

Fig. 13 illustrates the variation of coupled magnetic field strength with the rotation angle of the high-intensity magnet under conditions of one, two, and three casings. The results indicate that the coupled magnetic field strength increases significantly as the number of casings increases.

Within a single rotation cycle, the magnetic field curves corresponding to different casing numbers exhibit phase differences. Notably, the fundamental frequency of the magnetic signal remains unchanged regardless of the number of casings; only amplitude modulation and phase shifts occur. Under excitation by the time-varying magnetic field, the induced field generated by high-permeability casings preserves the same response frequency as the source field. The increase in casing number alters the system's equivalent parameters, leading to vector superposition of induced and source fields in space and resulting in an overall phase shift of the waveform. Therefore, although the coupled magnetic field signal exhibits amplitude enhancement and phase displacement, its frequency remains sinusoidal without distortion. This property ensures the reliability and interpretability of the coupled magnetic signal as a basis for casing identification, providing a solid theoretical foundation for downhole casing detection methods based on magnetic field characteristics.

4.3.4. Positioning angel and inter-casings angle

The polar relationship between the z-axis magnetic field strength and the rotation angle under different positioning angle θ ranging from 0° to 360° is shown in Fig. 14.

As shown in Fig. 14, with the variation of the positioning angle θ, the time-domain curves of the z-axis magnetic field strength undergo equal-angle phase shifts. This confirms that the induced magnetic field of the casing, located at different positions along an equal-radius circumferential circle of the magnetic source, follows the periodic variation of the source field. The trough position φ is obtained at θ, which satisfies Eq. (13). This indicates that when the magnetic north pole directly faces the casing axis, the coupled magnetic field strength at the observation point is enhanced in the negative direction. For positioning angle θ within the ranges of 0°–180° and 180°–360°, the amplitudes of the z-axis magnetic field time-domain curves remain identical, while their phases exhibit opposite variations. This phenomenon reflects the inherent symmetry of the spatial magnetic field distribution. It is worth noting that due to the spatial symmetry of the rotating magnetic field, the total magnetic field strength values on both sides of the permanent magnet's N-S poles are identical, but their vector directions are opposite. Therefore, when analyzing angles θ and α, the z-axis magnetic field strength is selected as the discriminating criterion instead of the total magnetic field strength. This enables accurate identification and assessment of the casing's magnetization characteristics across the full 360° circumferential range.

$$\varphi = \theta \tag{13}$$

In the case of two casings, the relationship between the z-axis time-domain curve amplitude and the trough position with respect to the casing intersection angle is shown in Fig. 15. As illustrated in Fig. 15, with the increase of inter-casings angle α, the z-axis magnetic field strength gradually decreases. When $\alpha = 180°$, when the line connecting the two casing axes is parallel to the axis of the high-intensity magnet, the z-axis magnetic field strength drops to zero. The trough position φ satisfies Eq. (14). This indicates that, unlike the single-casing scenario, when two casings

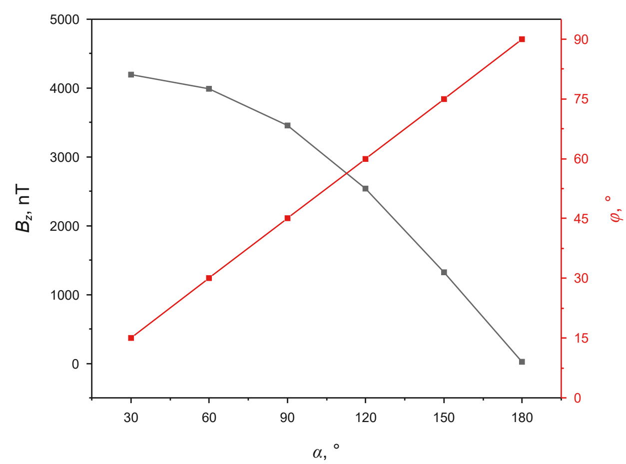

Fig. 15. Variation of z-axis curve trough value and its phase at different inter-casings angle.

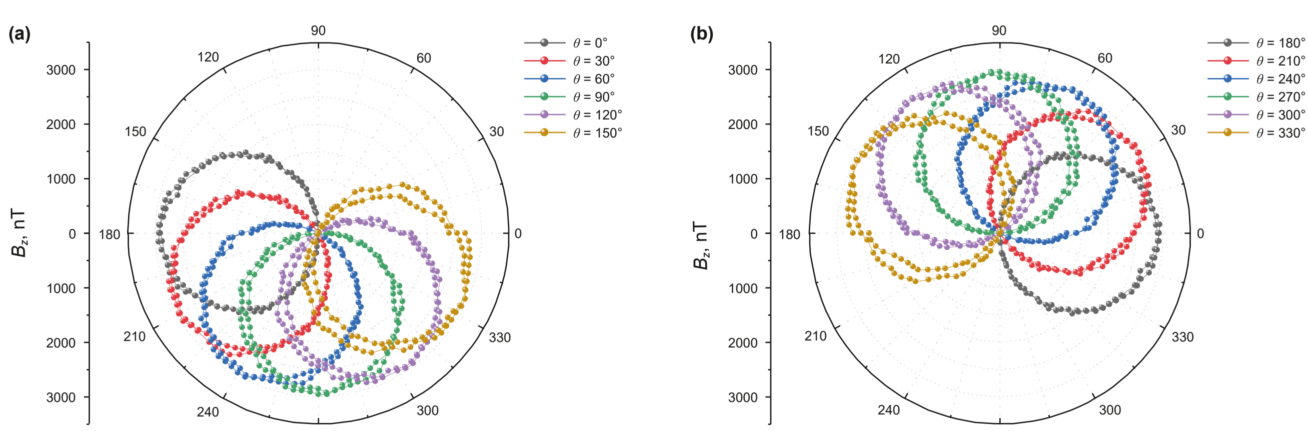

Fig. 14. Variation of z-axis magnetic field strength with rotation angle at different positioning angle: (**a**) θ: 0°–80° and (**b**) θ: 180°–360°.

exist around the drilling well, the coupled magnetic field strength at the observation point decreases when the magnetic north pole faces the midpoint of the casing intersection angle. This phenomenon demonstrates that the relative orientation of casings can be reflected in the *z*-axis magnetic field curve.

$$\varphi = \frac{\alpha}{2} + \theta \tag{14}$$

4.4. Coupled magnetic field in the geomagnetic environment

In practice, the geomagnetic field is a non-negligible component that couples with the casing's magnetization field and the background field. However, since the geomagnetic direction remains constant and its magnetization effect on the casing is limited to a range of approximately 0.5 m, the coupling between the geomagnetic field and the background field does not vary with different spatial distributions of the casings. Therefore, the geomagnetic north direction can be determined based on the coupling effect of the geomagnetic and background field. After filtering out the geomagnetic component, the relative orientation of the casings can be inferred according to the magnet–casing coupling mechanism.

Fig. 16 presents the time-varying curve of the three-axis combined total magnetic field strength over a complete cycle from 0° to 360° under a rotation frequency of 1 Hz. The original time-domain magnetic field signal is converted to the frequency domain using the fast Fourier transform (FFT):

$$B(f) = F\{B(t)\} \tag{15}$$

During the magnetization of the casing by the high-intensity magnet, the induced casing magnetic field couples with the magnetic field of the source itself. Fig. 16(a) shows the frequency spectrum response of this coupled magnetic field in the presence of the geomagnetic field, while Fig. 16(b) presents the spectral characteristics in the absence of geomagnetic influence. Comparison of Fig. 16 indicates that the introduction of the geomagnetic field adds a 1 Hz component to the spectrum, whereas the amplitudes of the 2 Hz signal and the DC component remain unchanged.

Analysis reveals that the DC component in the three-axis combined total magnetic field strength originates from the intrinsic field of the high-intensity magnet, the 2 Hz signal corresponds to the dynamic response induced by the casing magnetization, and the 1 Hz signal arises from the coupling effect of the geomagnetic field. Based on these spectral features, the magnetic north direction can be further determined. By analyzing the phase of the periodic time-series curve, the orientation of magnetic north relative to the coordinate system can be established, providing a reference for casing localization. Since the magnetic field component along the axial vertical direction is opposite to the north pole direction of the high-intensity magnet, when the north pole rotates to align with the horizontal component of the geomagnetic field, the spatial magnetic field strength reaches its minimum. At this point, the phase angle (ω) corresponding to the trough of the total magnetic field signal indicates the direction of geomagnetic north in the coordinate system. In Fig. 16(a), the trough of the total magnetic field signal occurs at 0.125 s, corresponding to 45° within one cycle, thus indicating that the geomagnetic north direction in the coordinate system is located at 45°.

Since the geomagnetic field strength is significantly higher than the casing-induced magnetic field, and the casing magnetization field exhibits a sinusoidal signal centered around zero, the vertical component of the geomagnetic field can be determined by

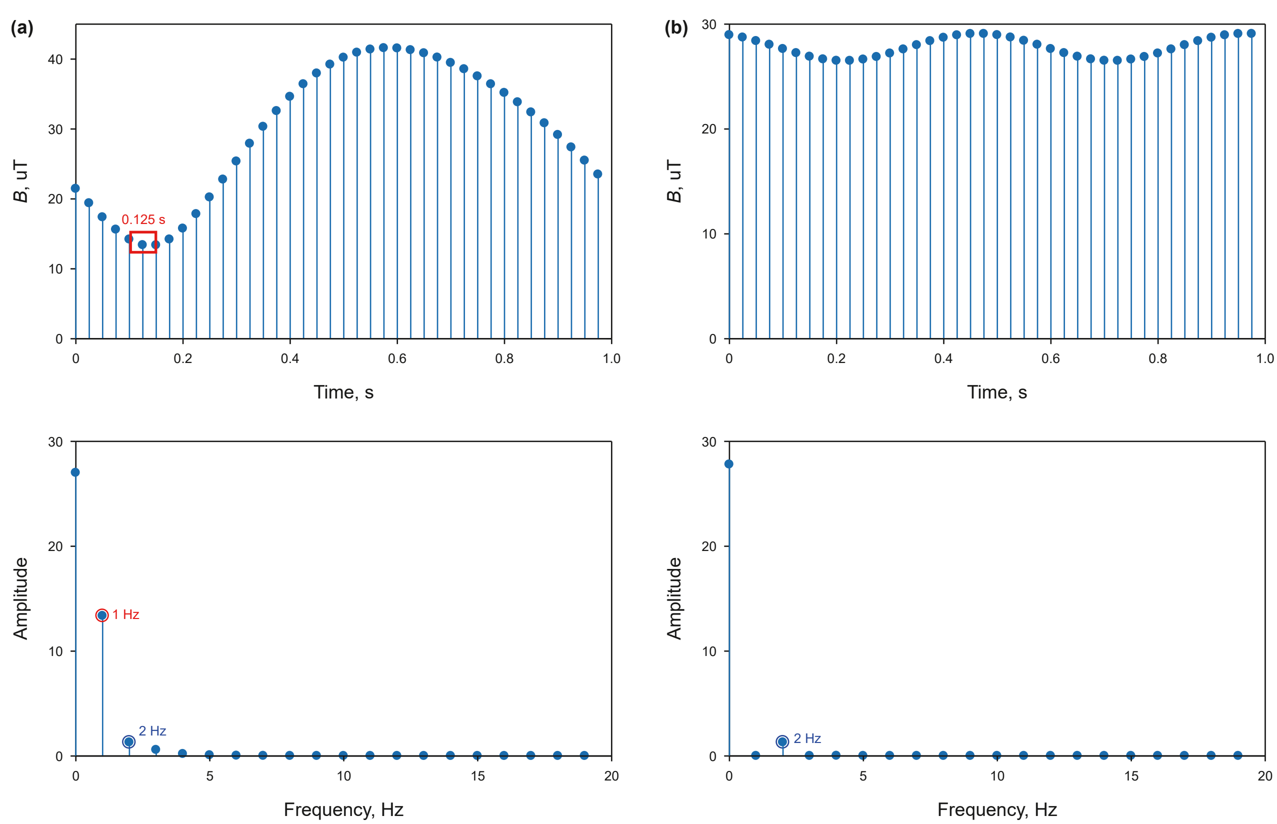

Fig. 16. Time-domain magnetic field signals and their spectra: (**a**) including geomagnetic and (**b**) excluding geomagnetic.

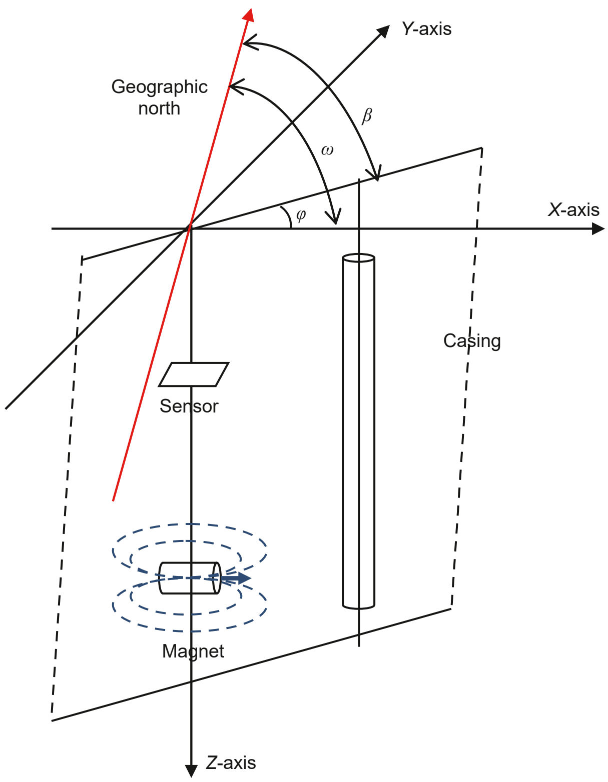

Fig. 17. Schematic diagram of casing positioning method.

analyzing the baseline offset of the z-axis magnetic field relative to zero. By applying a band-pass filter (1 Hz passband: 0.9–1.1 Hz), the geomagnetic field signal can be extracted to accurately determine its intensity and direction in the horizontal plane. Subtracting the geomagnetic field components from the measured three-axis magnetic field data effectively eliminates geomagnetic interference, yielding the three-axis magnetic field strength generated solely by the magnet and the casing magnetization. Based on this result, the relative orientation of the casings can be further determined, and by combining it with the geomagnetic north reference, the precise localization of the casings can be achieved. The overall positioning method is illustrated in Fig. 17, and the casing azimuth (β) is calculated using Eq. (16) finally. The signal processing flowchart is shown in Fig. 18.

$$\beta = \omega - \varphi \tag{16}$$

5. Establishment of a casing positioning model under coupled magnetic field

5.1. Determination of observation point location

As discussed in Section 4.3.1, the time-domain curves of the magnetic field at different observation points exhibit phase shifts. Since the phase shift is strongly correlated with the casing orientation, optimizing the observation point location is necessary to achieve unique orientation identification. Taking the case of two casings with a casing intersection angle of $\alpha = 60°$ as an example, the relationship between the z-axis magnetic field strength and the rotation angle at different observation points, with the casings located 2 m away, is shown in Fig. 19.

As shown in Fig. 19, when the casing distance $d = 2$ m, the signal phases at the observation points are consistent, provided that the observation point positions satisfy $H_p \geq d$. Simulations were conducted for casing distance of 2, 3, and 4 m, as well as varying casing quantities, with observation points spaced at 100 mm intervals using the same method. The phase consistency of observation point signals exhibited similar patterns, but the minimum observation

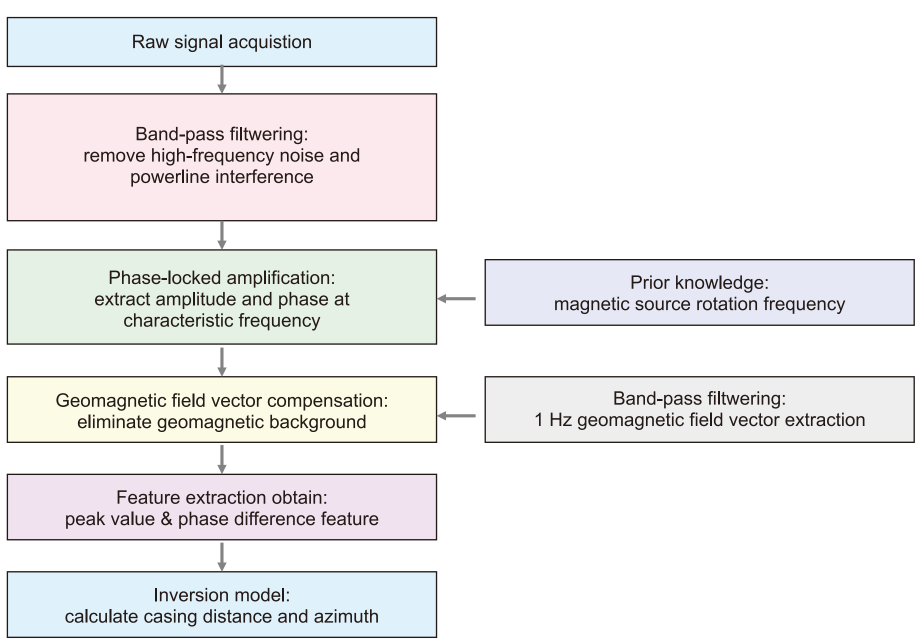

Fig. 18. Signal processing flowchart.

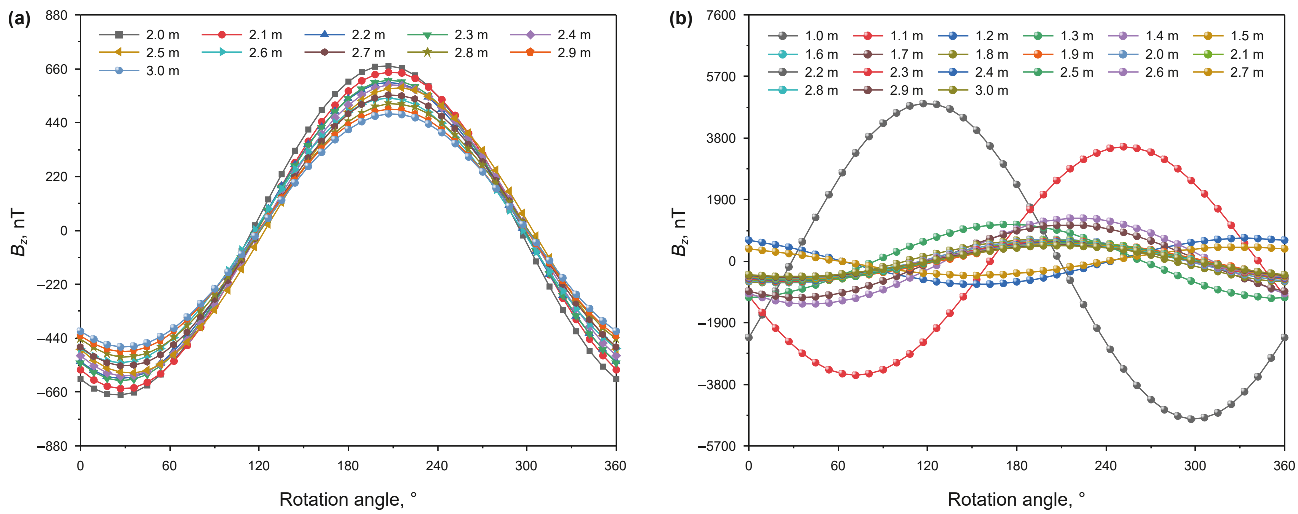

Fig. 19. Variation in *z*-axis magnetic field strength at different observation points: (**a**) $d = 2$ m; H_p: 2–3 m and (**b**) $d = 2$ m; H_p: 1–3 m.

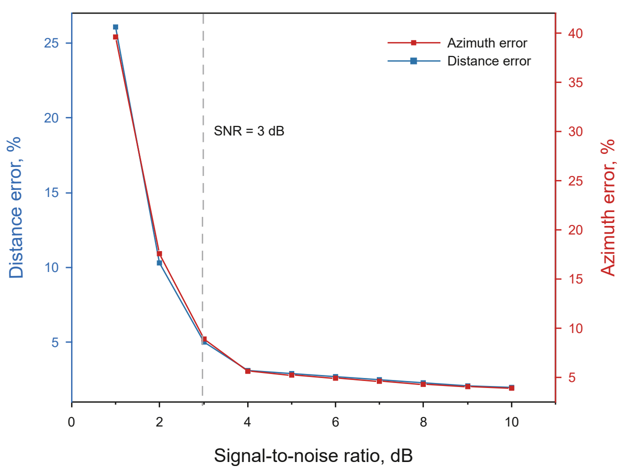

Fig. 20. Positioning error at different signal-to-noise ratios.

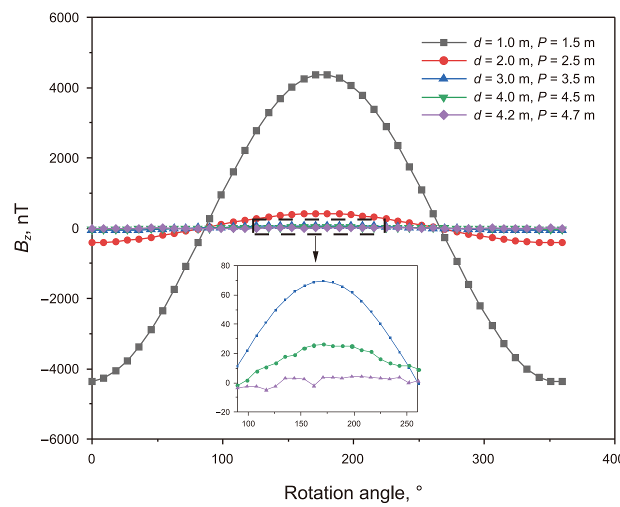

Fig. 21. Variation in *z*-axis magnetic field strength at different observation point and casing distance.

point position showed deviations within 0.5 m, min $(H_p) = d + \Delta_p$ ($0 \text{ m} \le \Delta_p \le 0.5$ m). Therefore, to accurately measure the casing orientation, the condition $H_p \ge d + 0.5$ m must be satisfied.

To ensure the validity of the magnetic field signal, the signal-to-noise ratio was adopted as the discrimination criterion, where the ratio of signal power to noise power must satisfy SNR ≥ 3.

$$\mathrm{SNR} = \frac{A^2/2}{\sigma^2} \tag{17}$$

where A represents the magnetic field strength amplitude and σ^2 denotes the noise variance.

By superimposing Gaussian white noise of varying intensities onto the simulated signal, the positioning performance under different signal-to-noise ratio conditions was simulated. The results are shown in Fig. 20. Analysis indicates that this method demonstrates excellent robustness. When the signal-to-noise ratio exceeds 3 dB, the distance inversion error remains stably within 2%. Even when the signal-to-noise ratio drops to 3 dB, the average errors for distance and bearing are still controlled within 5% and 7%, respectively, enabling effective collision-avoidance positioning.

When the casing is located at a large distance, its induced magnetization field intensity decays significantly. In this case, the influence of geomagnetic noise fluctuations must be considered, as such noise can distort low-amplitude sinusoidal magnetic signals. The maximum amplitude of typical geomagnetic noise can reach up to 10 nT (Liang et al., 2013), requiring that the effective signal amplitude be at least 24.5 nT. Numerical simulations were conducted using a single casing, as the coupling magnetic field strength for a single casing is lower than that for multiple casings; therefore, if the signal remains undistorted for a single casing, it will also satisfy the condition for multiple casings. The casing distance were set to 1, 2, 3, 4, and 4.2 m, with observation points located at 1.5, 2.5, 3.5, 4.5, and 4.7 m, respectively. After superimposing 10 nT noise, the results are shown in Fig. 21. As observed in Fig. 21, when the casing distance increases to 4 m, the *z*-axis magnetic field strength is 26.183 nT, satisfying the SNR requirement. However, for casing distance greater than 4 m, the signal becomes distorted. Therefore, the maximum detectable distance is 4 m, with the observation point constrained to be beyond 4.5 m along the axial direction. Based on the magnetic field attenuation

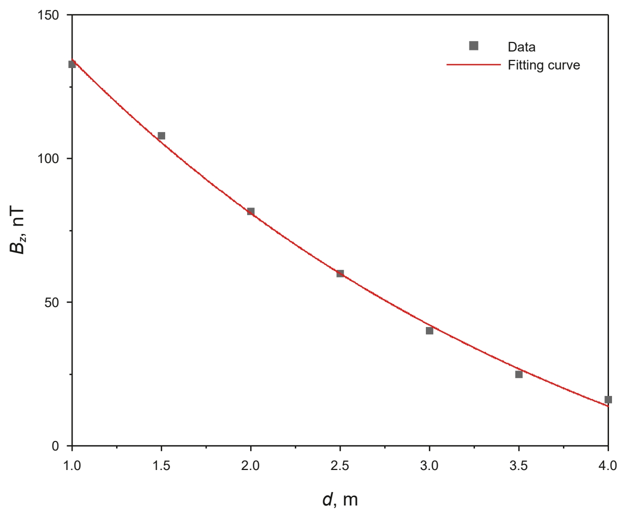

Fig. 22. Variation in z-axis magnetic field strength at difference casing distance.

(ExpDel) was used for fitting, yielding a corresponding fitting formula. The casing distance can then be inversely calculated based on this fitted relationship.

$$B_z = 269.34e^{\frac{-d}{3.1349}} - 61.41 \tag{18}$$

When two casings are present around the drilling well, the relationship between B and B_Z with respect to α are shown in Fig. 23. Gaussian and Extreme functions were used for curve fitting, yielding the corresponding fitting Eq. (19):

$$\begin{cases} B = y_1 + A_1 e^{-\frac{(\alpha - w_{c1})^2}{2{w_1}^2}} \\ B_z = y_2 + A_2 \cdot e^{1-e^{\frac{-(\alpha - w_{c2})}{w_2}}} \end{cases} \tag{19}$$

Among these, $\omega_{c1} = 87.70$, $\omega_{c2} = 240.71$, and remaining parameters are each related to variable d. After linear fitting, they are uniformly transformed into expressions for variable d. Finally, substituting these into the overall fitting Eq. (20)

$$\begin{cases} B(d,\alpha) = \dfrac{\left(-1469425.62e^{\frac{-d}{0.69442}} + 2966.93\right)}{\left(76.28214 + 11.45095d - 1.1489d^2\right) \times \sqrt{\frac{\pi}{2}}} \cdot e^{\frac{-2\times(\alpha - 87.67)^2}{\left(76.28214 + 11.45095 \cdot d - 1.1489 \cdot d^2\right)^2}} + 18481.57004e^{\frac{-d}{0.62459}} + 3.99239 \\ B_z(d,\alpha) = 343.12 - 135.36d + 13.92d^2 + \dfrac{1}{-0.0034 - 4.58d^{4.81}} e^{1-e^{\frac{-(\alpha - 240.71)}{52.06 + 41.22d}}} \end{cases} \tag{20}$$

characteristics, setting the observation point at 4.5 m maximizes the retention of effective magnetic signal amplitude.

5.2. Relative calculation model for casing distance and azimuth

When a single casing is present around the drilling well, the casing distance were set to 1, 1.5, 2, 2.5, 3, 3.5, and 4 m. The relationship between the peak z-axis magnetic field strength and the casing distance is shown in Fig. 22. An exponential decay function

To determine the casing azimuth, the three-axis components of the magnetic field signal over a complete rotation cycle (0°–360°) must be extracted. First, the phase angle corresponding to the trough of the total magnetic field is used to determine the direction of geomagnetic north relative to the x-axis. After filtering out the geomagnetic component, the relative position of the casing is determined based on the magnet–casing coupling mechanism, and the casing azimuth β is then obtained, according to Eq. (16). Since the x-axis magnetic field signal always reaches its maximum

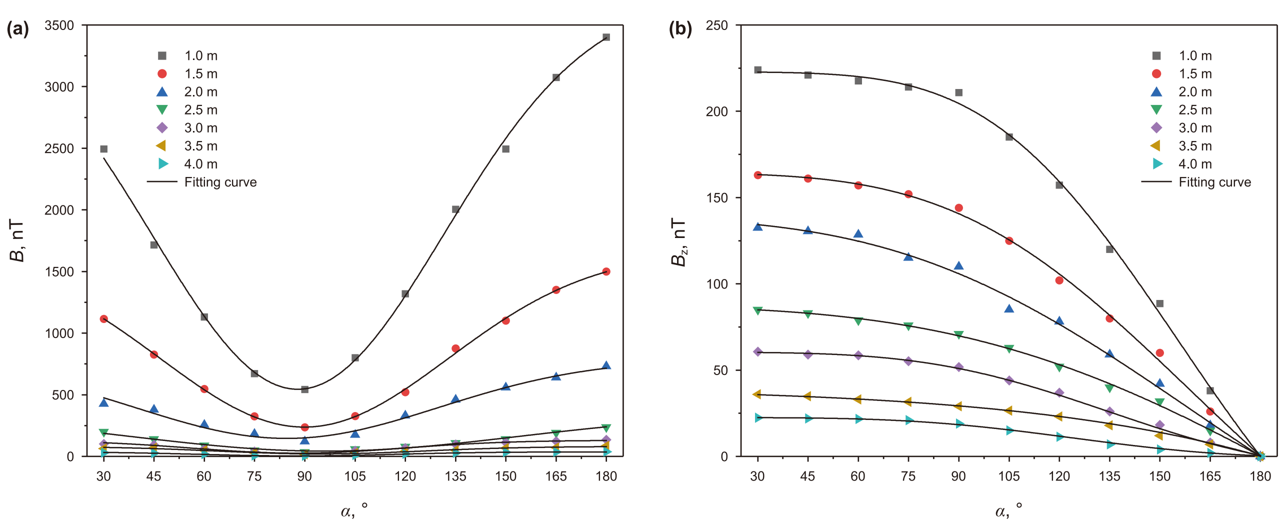

Fig. 23. Changes in magnetic field values at different casing distance and inter-casings angle: (**a**) total magnetic field and (**b**) z-axis magnetic field.

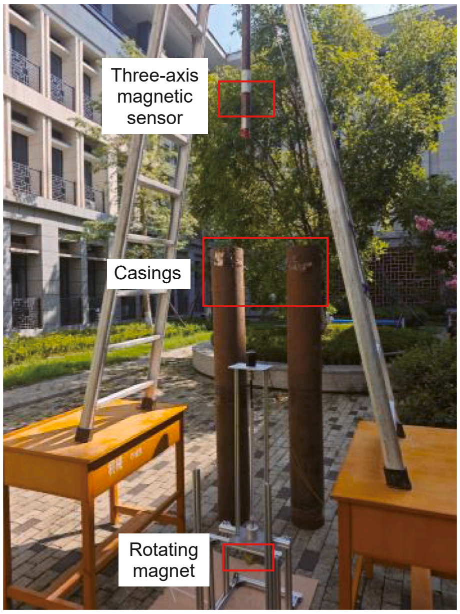

Fig. 24. Experimental platform setup.

Table 3
Experimental parameters reference values.

Parameters	Value
Casing heigh H_c, mm	2000
Casing number n	2
Casing distance d, mm	1000
Inter-casing angle α, °	30
Observation point height H_p, mm	2300

Table 4
Experimental equipment.

Experimental parameters	Properties	Value
Measuring probe	Accuracy, N·m	0.10%
	Sample frequency, Hz	2.6
High-intensity magnet	Magnetization, A/m	6.5×10^5
	Diameter, mm	80
	Length, mm	100
	Model number	N35
Casing	Outer diameter, mm	244.5
	Thickness, mm	10
	Height, mm	1000
Electric motor	Frequency, Hz	0–3000
	Power, w	30

negative value at the 0° position in the coordinate system (where the high-intensity magnet's pole aligns with the x-axis), this point corresponds to the curve trough and is taken as the phase reference (0°). One full rotation from this reference constitutes the complete target magnetic signal.

For single-casing positioning, first substitute measurement data into Eq. (18) to obtain d, then calculate θ using Eq. (13). For dual-casing scenarios, substitute measurement data into Eq. (20) to obtain d and α, then calculate θ using Eq. (14). Thus, the relative casing orientations are θ and $\theta + \alpha$.

6. Experimental results

To validate the accuracy of finite element numerical simulation results, ground-based simulation experiments were conducted to study the magnetization of multiple closely spaced casings under alternating magnetic field. To eliminate interference from ferromagnetic materials in the environment, the experiments were conducted in an open outdoor area. The experimental platform, excluding the motor, was constructed entirely from aluminum alloy. The existing three-axis magnetic field sensors embedded within the probe tube served as the magnetic field signal acquisition devices. The distance and angle between casings could be directly read from markings on the drawings. The probe tube and high-intensity magnet were suspended coaxially in the air. By positioning the casing at different spatial locations, an equivalent vertical drilling test scenario was constructed, as shown in Fig. 24. Table 3 reports the experimental parameters reference values, and Table 4 reports experimental equipment.

Given that the high-intensity magnet used in the experiment has a magnetic flux density of 6.5×10^5 A/m, the distance between the sensor and the magnetic source required to achieve a 2 m detection range, as derived in Section 5.1, reaches 2.3 m. The experimental monitoring data curves are shown in Fig. 25(a). The measured curves exhibit sinusoidal variations consistent with the simulation results, where the z-axis sinusoidal fluctuations accurately reflect the magnetization effect of the rotating high-intensity magnet on the casing. The differing peak-to-peak values along the x and y axes indicate that the interference characteristics of the casing on the magnetic signal are detectable. Although the downhole magnetic sensor incorporates built-in hardware filtering, residual interference still causes slight waveform distortion at the peaks.

Prior to data acquisition, free-space magnetic field calibration was performed in a non-casing environment. Repeated measurements were conducted to establish a baseline value under the combined influence of the geomagnetic field and the magnetic source, thereby providing a numerical reference for subsequent magnetization field analysis. Using the average of the three-axis magnetic field components as the baseline, the measured data were subjected to translation and detrending processing. This yielded absolute fluctuation values referenced to zero, which served as the raw amplitude encoding of the alternating magnetic field.

On this basis, magnetization response experiments were carried out under various casing spatial distributions. Following the procedure outlined in Section 4.4, the geomagnetic component was filtered out from the measurements. A comparison between measured and theoretical values enabled the establishment of a mapping relationship between the zero-referenced magnetic field data and the theoretical magnetic field strength (Hu et al., 2025), ultimately yielding the true magnetic field response. A typical magnetic field response curve over one cycle is shown in Fig. 25(b).

Based on the specific parameters of the experimental environment, a numerical simulation model consistent with the environmental data was established. By varying the casing angle α and distance d, the attenuation trend of the z-axis magnetic field strength was obtained. As shown in Fig. 26(a) and (b), this trend matches the simulation results, with a maximum deviation of 65.7 nT and a maximum relative error of 8.3%. Fig. 27(a) and (b) show that the experimental results exhibit the same trend as the simulation, with a maximum deviation of 106.5 nT and a maximum relative error of 10.5%. The errors primarily arise from slight deviations between the actual casing center and the theoretical center when adjusting the measurement distance and angle.

These discrepancies indicate that the experimental results are generally consistent with the simulation, with identical magnetic field variation patterns and only minor numerical differences, thereby validating the accuracy of the finite element simulations.

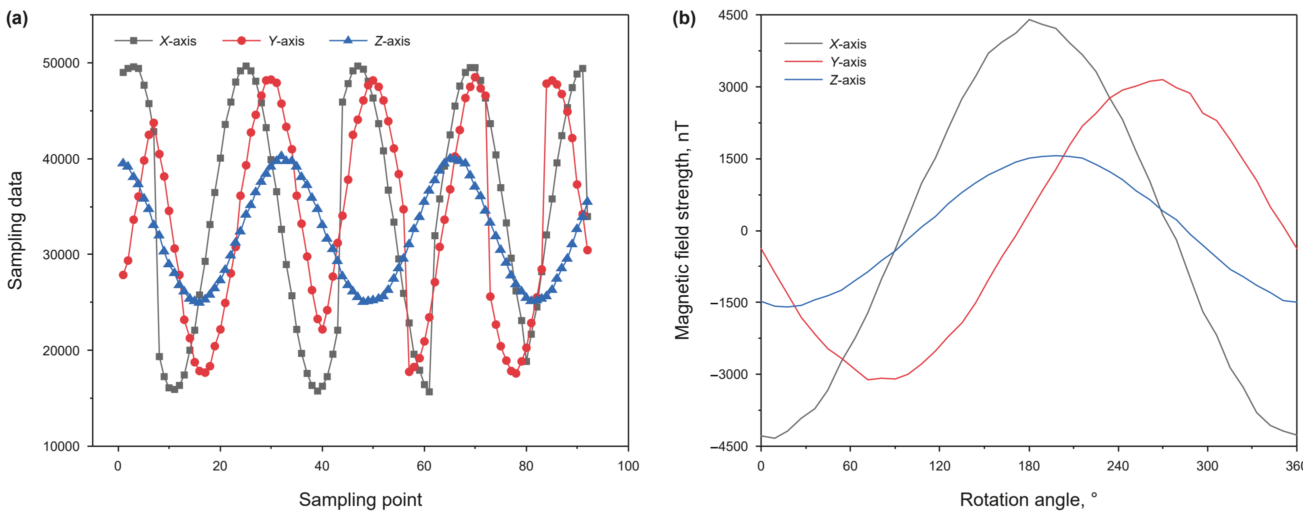

Fig. 25. Magnetic field data: (**a**) measurement data and (**b**) filter data.

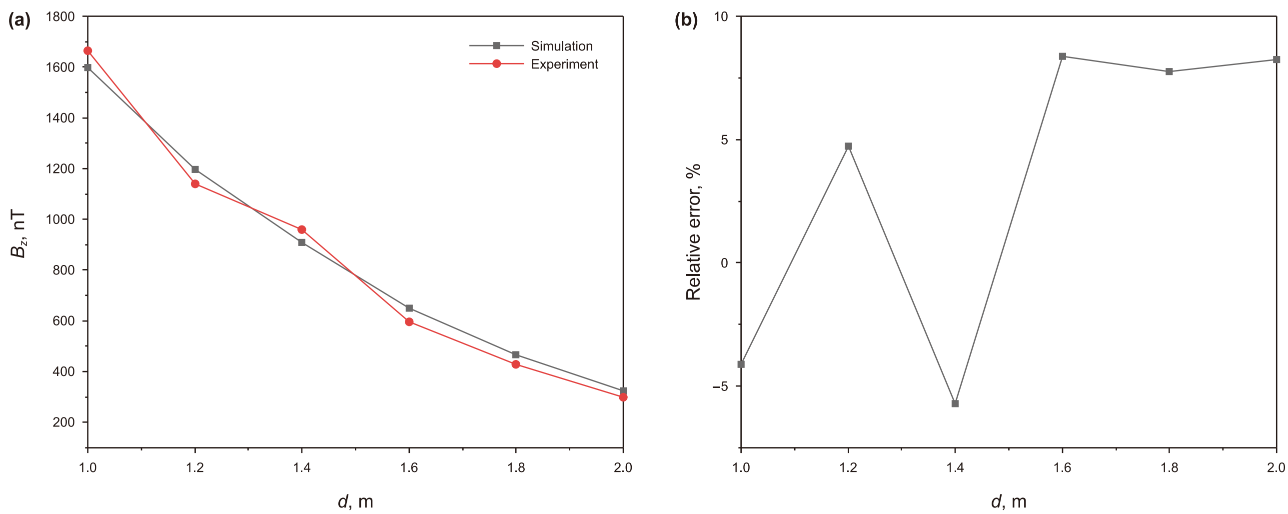

Fig. 26. Comparison of experimental and simulation results: (**a**) distance change and (**b**) relative error in distance change.

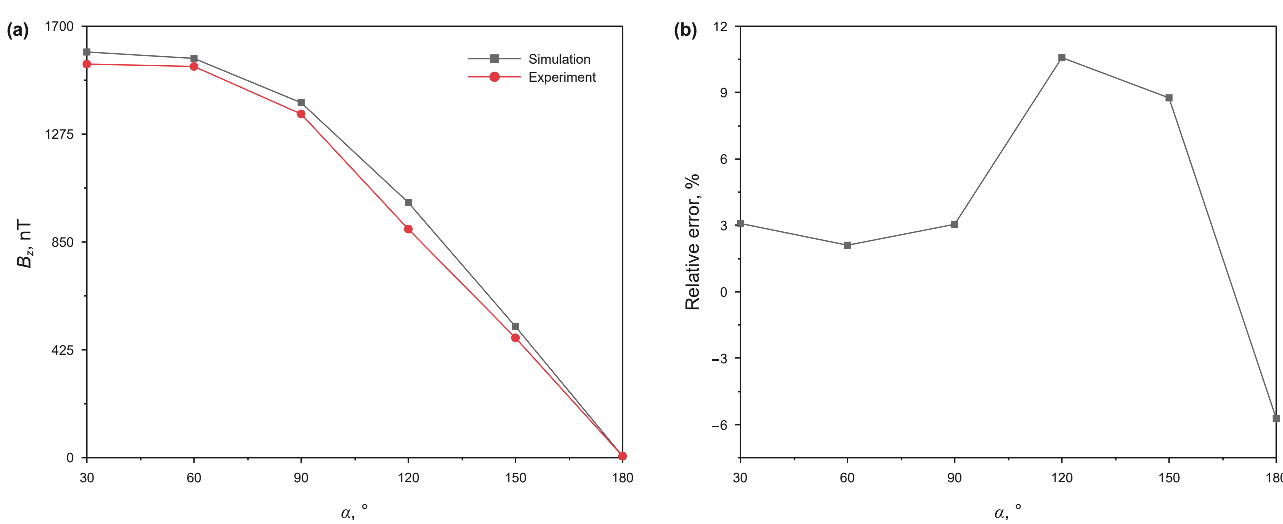

Fig. 27. Comparison of experimental and simulation results: (**a**) inter-casing angle change, (**b**) relative error in inter-casings angle change.

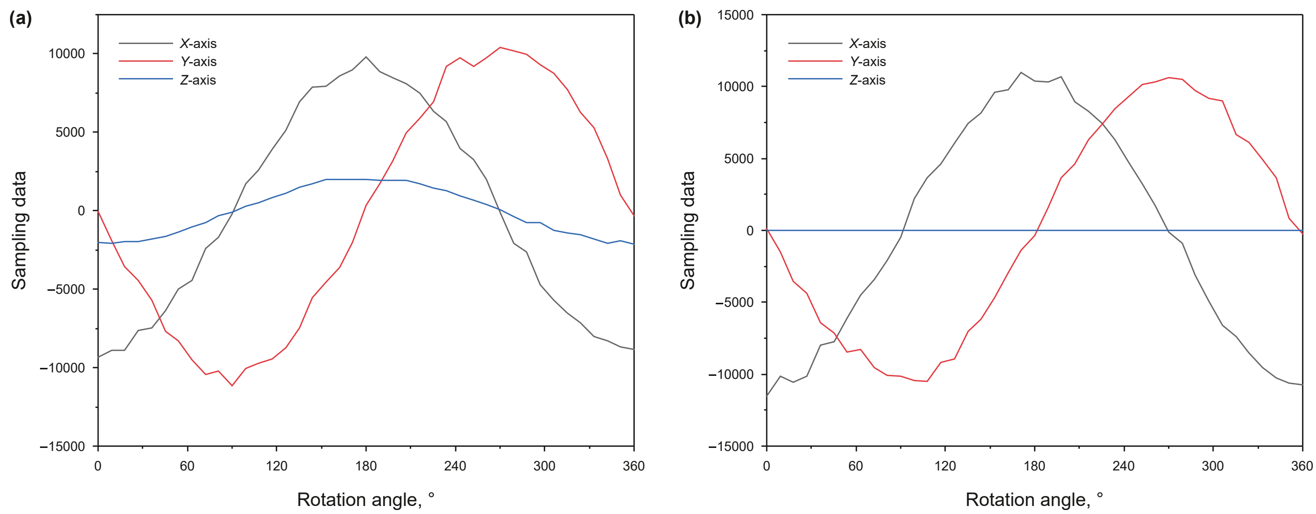

Fig. 28. Different scenarios: (**a**) three casings and (**b**) four casings.

Table 5
Comparison of measured and calculated results.

n	Actual location			Measured value				Calculated location			Absolute error	
	Azimuth β, °							Azimuth β, °				
	Casing A	Casing B	d, m	B_z, nT	B, nT	φ, °	ω, °	Casing A	Casing B	d, m	β_{max}, °	d, m
1	40	/	1.6	427.96	/	2.03	41.32	39.29	/	1.62	0.71	0.02
1	10	/	1.6	439.08	/	31.06	42.56	12.5	/	1.61	2.5	0.01
1	340	/	1.6	456.04	/	61.32	42.63	341.31	/	1.58	1.31	0.02
1	40	/	1.2	803.01	/	2.43	42.02	39.59	/	1.25	0.41	0.05
1	10	/	1.2	868.37	/	30.96	42.99	12.03	/	1.21	2.03	0.01
1	340	/	1.2	916.39	/	61.71	41.32	339.61	/	1.17	0.39	0.03
2	70	310	1.6	413.1	97.08	29.27	42.12	72.12	313.07	1.57	3.07	0.03
2	340	280	1.6	576.92	79.19	92.55	39.89	338.89	275.78	1.62	4.22	0.02
2	280	250	1.6	620.1	113	138.19	42.53	281.03	247.65	1.65	2.35	0.05
2	70	310	1.2	750.37	348.33	29.52	38.06	68.06	309.51	1.23	1.94	0.03
2	340	280	1.2	1163.2	761.01	92.26	43.41	340.41	279.89	1.15	0.41	0.05
2	280	250	1.2	1095.5	779.1	138.01	42.91	281.41	248.38	1.28	1.41	0.08

Table 6
Comparison of different electromagnetic positioning methods in recent years.

Method	Requires adjacent well operation?	Max. detection range	Applicable casing scenario	Positioning accuracy	Cost and complexity
Method proposed by this paper	No	4 m	Multiple casings	High; decouples multi-casing interference via amplitude and phase analysis	Low; simplified operation without surface equipment or adjacent well tools
Current excitation method of Yan et al. (2022)	Yes; requires current injection tool in adjacent well	>5 m	Multiple casings	High; stable EM signal, yet limited by tool accuracy	High; requires complex surface power source, increasing cost and time
Magnet force method of Hu and Fu (2023b)	No; magnets are deployed on BHA	1 m	Single casing	Moderate; high accuracy at close range but significant attenuation with distance	Moderate; requires at least 8 powerful magnets spaced along the drill collar
Dual magnetic source method of Dou et al. (2018)	No; requires internal magnetic source deployment	~3 m	Single casing	High; suitable for single source-casing interaction	High; internal source deployment increases complexity and cost
Traditional passive magnetic method	No; relies on casing remnant magnetism	~2 m	Single casing	Low; weak remnant signal susceptible to tool noise and geomagnetic anomalies	Low; simple tool but poor accuracy

Three and four casings were distributed at 90° intervals. The spatial magnetic field data collected over one cycle (0°–360° in the plane coordinate system) is shown in Fig. 28. Experimental results indicate that the total magnetic field strength increases with the number of casings, consistent with numerical simulations and theoretical expectations. In Fig. 28(a), the *z*-axis magnetic field curve reaches its maximum at a phase angle of 180°, coinciding precisely with the moment when the high-intensity magnet's poles rotate to point toward the middle casing among the three. This confirms the method's applicability for locating and identifying two or more casings. In Fig. 28(b), the *z*-axis magnetic field curve exhibits a stable amplitude of zero. Due to the spatial distribution characteristics of the N-S magnetic poles, when four casings are spatially symmetrically distributed, the coupled magnetic fields cancel each other out. This also satisfies theoretical predictions, verifying the engineering applicability of the method in multi-casing scenarios.

Due to the complex magnetic coupling mechanisms involving three or more casings, establishing a unified computational model using empirical fitting formulas not only substantially increases the computational burden but may also introduce additional errors. Therefore, the casing positioning model proposed in this study is primarily designed for scenarios involving one or two casings. For more complex multi-casing scenarios, future work will explore artificial intelligence approaches, such as deep learning, to develop an inversion model that correlates the coupled magnetic field with the spatial distribution of multiple casings.

Following the method described in Section 5.2, the spatial magnetic field calculation equations for the casing at different distance and orientations were derived when the high-intensity magnet's magnetization strength is 6.5×10^5 A/m. With one casing present around the drilling well, the equation for the peak *z*-axis magnetic field strength as a function of casing distance is:

$$B_z = 5849.48\mathrm{e}^{\frac{-d}{0.66617}} - 83.28125 \tag{21}$$

With two casings present around the drilling well, the positioning calculation equation is:

$$\begin{cases} B = \left(\dfrac{-136998.31 + 69307.57d}{(96.975d - 65.65) \times \sqrt{\dfrac{\pi}{2}}} \right) \cdot \mathrm{e}^{\frac{-2\times(\alpha-98)^2}{(96.975d-65.65)^2}} - 1748.55d + 3073.05 \\ B_z = (162.28 - 238.55d) \cdot \mathrm{e}^{\frac{-\alpha}{(63.52-114.3d)}} - 1044.75d + 2646.03 \end{cases} \tag{22}$$

For scenarios with one or two casings at different orientation and distance, the casing azimuth (β) and distance (d) were calculated using Eqs. (13), (14), (16), (21) and (22). The results are shown in Table 5. Among these, casing A and casing B are identical in material and dimensions, with material parameters listed in Table 5 and n denotes the number of casings.

As shown in Table 5, the maximum absolute error in orientation calculation for a single casing is 2.5°, and the maximum absolute distance error is 0.05 m. For dual casings, the corresponding errors are 4.22° in orientation and 0.08 m in distance. Both the angular and distance errors remain at a low level, demonstrating that the method can accurately determine the relative orientation and distance of the casing.

7. Discussion

Selecting high-intensity magnets with higher magnetization strength and increasing magnet diameter can enhance detection range. However, the selection range for high-strength high-intensity magnets is limited, with the current maximum magnetization strength only reaching approximately 1.2×10^6 A/m (Wang et al., 2003; Zhao and Huang, 2006). Additionally, magnet diameter design is constrained by drill string dimensions. Implementing either of these options to improve detection range presents significant challenges. Radially stacking high-intensity magnets within the drill string can enhance magnetization strength and expand detection range. However, the number of magnets is difficult to significantly increase due to geometric constraints imposed by the wellbore and drill string dimensions. Adopting a magnetic short section structure along the drill string axis can be equivalent to the linear superposition of a single magnet, thereby overcoming the quantity limitation. However, mutual magnetic interference exists between magnets within the magnetic short section. It is necessary to clearly define the effective influence zone of the linearly superimposed magnetic field and reasonably determine the installation position of the three-axis magnetic field sensor accordingly.

Compared to existing techniques that rely on measuring magnetic flux density to determine adjacent casing positions, this paper proposes a method based on magnetizing adjacent casing using fixed-axis rotating magnets. By analyzing the time-series characteristics of the coupled magnetic field, a mapping relationship is established between the field and the complex multi-casing spatial structure, enabling the determination of distance and relative orientations among multiple casings. This method further utilizes the geomagnetic field to determine the geomagnetic north direction, ultimately resolving the geomagnetic orientation of the casing.

A systematic comparison between the proposed method and other major electromagnetic positioning methods is presented in Table 6. The current maximum detection range is 4 m, which is slightly shorter than that of current excitation methods, and requires further optimization of magnetic strength or sensor sensitivity. Existing methods typically determine the casing azimuth relative to geomagnetic north by measuring the angle between a reference plane and the magnetic tool face (MTF) in the MWD system, using static magnetic field measurements (Eq. (23)). The approach presented in this study leverages the coupling between the geomagnetic field and the rotating dynamic magnetic field to indicate geomagnetic north, effectively avoiding magnetic interference from ferromagnetic materials and enabling accurate casing positioning.

$$\mathrm{MTF} = \arctan\left(\frac{B_y}{B_x}\right) \tag{23}$$

This study presents a theoretical innovation through the establishment of a novel active magnetic logging framework that systematically addresses three fundamental challenges: multi-casing magnetization, signal separation, and inversion. The key contributions are: First, compared to the static conduction model relied upon by current excitation methods, which are susceptible to constraints from current shunting and signal confusion (Yan et al., 2022; Dou et al., 2024), the proposed rotating magnetic field dynamic magnetization mechanism transforms each casing into an independent magnetic source through alternating excitation, achieving a leap from “static parameters” to “dynamic enhancement”. Second, unlike dual-source magnetic systems requiring predefined relative positions of magnetic sources (Dou et al., 2018), the spatiotemporally coupled inversion algorithm constructed by this method simultaneously solves for multiple target distances and azimuths based solely on single-point sequential magnetic field data, eliminating reliance on prior geometric relationships. Third, at the signal processing level, the introduced phase-synchronized demodulation method overcomes the inherent limitations of traditional amplitude analysis in multi-source superimposed fields by assigning “phase tags” to each casing response (Liu et al., 2020; Wu and Wei, 2020), thereby systematically establishing a novel theoretical paradigm for multi-casing localization in densely clustered wells.

In magnetic positioning methods, raw data collected by three-axis magnetic sensors must undergo signal extraction and data transformation processes, typically involving filtering, frequency-domain transformation, and signal separation. Each of these steps may introduce errors that affect final positioning accuracy. Therefore, developing high-precision, high-robustness signal processing algorithms to ensure effective magnetic signal extraction is key to improving the reliability and accuracy of this method.

This study not only provides theoretical guidance for the development of anti-collision well trajectory measurement and control technologies but also addresses significant engineering demands and applications in rescue well communication, storage well re-entry, and other scenarios where multiple close-range casings exist.

In actual cluster well engineering, the spacing between casing strings generally increases with depth. As a result, anti-collision positioning between adjacent wells is primarily concerned with the upper section of the well. Although this section is typically not subject to extreme temperature or pressure conditions, complex environmental factors arising from specific geological formations or drilling operations cannot be ruled out. Future work will focus on advancing the testing of this technology in simulated downhole environments or actual drilling scenarios to systematically evaluate its applicability and robustness under real conditions.

Detection distance directly affects sensor placement; for a high-intensity magnet with a magnetization of 1.2×10^6 A/m, the detection range is 4 m, requiring the sensor to be positioned at least 4 m from the magnet. However, space constraints of the drill string may pose challenges for sensor layout. Future research will optimize its integration into BHA configurations to develop compact, practical downhole tools.

This study focused on single- and dual-casing scenarios, laying the groundwork for future inversion studies to determine spatial positions from known magnetic field distributions. Subsequent research will establish models to calculate distance and orientations of multiple casings under various distributions, combining simulation and experimental data. By analyzing the spatial distribution of coupled magnetic field and applying machine learning methods, intelligent inversion algorithms can handle more complex multi-casing environments while improving interpretation efficiency and accuracy. Since the magnetic field feature parameters collected for different numbers of casings vary, a strategy of first classifying the number of casings followed by locating them is adopted. Specifically, a random forest model is first utilized for efficient classification of casing quantities. Subsequently, a multi-input regression model is constructed using a convolutional neural network (CNN) and a long short-term memory network (LSTM) to extract spatial structural features and temporal dynamic patterns from the magnetic field signals, respectively. This enables precise inversion of casing orientation and distance. Methodologically, this work draws upon successful approaches from related fields: CNN's capability in identifying road structures within complex georadar signals (Mojahid et al., 2025) and LSTM's effective application in underground electromagnetic data inversion (Shi et al., 2024) provide both theoretical and technical references for this model. By integrating extensive experimental measurements and numerical simulation data, and training the model with error metrics as the optimization objective, we ultimately constructed a deep learning-based multi-casing positioning prediction system that combines physical interpretability with environmental robustness. In deviated well applications, potential z-axis magnetic field offsets due to non-parallelism between drill string and casing axes must be considered; these can be corrected through simulation and experimentation, thereby extending the applicability of this method to deviated well environments.

8. Conclusions

This study addresses the critical need for anti-collision positioning of multiple closely spaced casings in cluster well drilling and proposes a novel active magnetic ranging method based on high-intensity magnet magnetization and magnetic field coupling analysis. Through systematic numerical simulations and experimental validation, the main conclusions are as follows:

(1) The study reveals the magnetic field coupling mechanism between rotating high-intensity magnets and multiple closely spaced casings. The presence of casings induces characteristic amplitude modulation and phase shifts in the spatially coupled magnetic field, exhibiting a clear mapping relationship with casing distance, azimuth, and quantity. This provides a theoretical foundation for casing positioning without requiring adjacent well operations.

(2) System performance boundaries are defined: at a high-intensity magnet flux density of 1.2×10^6 A/m, the maximum effective detection distance is 4 m. For accurate azimuth calculation, the magnetic field sensor must be installed such that $H_p \geq d + 0.5$ m (where H_p is the observation point height and d is the casing distance).

(3) Numerical simulations and experimental results demonstrate that within a detection range of 4 m, this method achieves accurate positioning for single and dual casings. The maximum absolute error in calculated casing azimuth is 4.22°, while the maximum absolute error in calculated distance is 0.08 m. Compared to existing methods, this approach enables effective sensing in multi-casing environments without requiring intervention from adjacent wells.

(4) This study offers a novel technical approach to resolving collision avoidance in high-density cluster wells, demonstrating strong engineering application potential. Subsequent research will establish a numerical model for magnetic field coupling when multiple casings are randomly distributed in space. It will investigate the impact of casing spatial orientation on magnetic field distribution characteristics, revealing quantitative relationships between tilt angle variations and magnetic field signature

changes. By integrating artificial intelligence methods such as deep learning (CNN, LSTM), coupled magnetic field and multi-casing spatial distribution inversion models were constructed. This enables high-precision simultaneous identification of casing quantity, distance, orientation, and posture in highly noisy environments. Concurrently, the magnetic response characteristics of casings with varying diameters and wall thicknesses under different combinations will be examined to enhance the model's applicability and robustness in real well conditions.

CRediT authorship contribution statement

Xu-Ping Ma: Writing – review & editing, Writing – original draft, Software, Methodology, Investigation, Conceptualization. **Zhong-Zhi Hu:** Validation, Supervision, Formal analysis. **Shao-Jie Fu:** Project administration, Funding acquisition. **Yu-Dian Lei:** Validation, Supervision.

Data availability

Data will be made available on request.

Declaration of competing interest

The authors declared no potential conflicts of interest with respect to the research, author-ship, and/or publication of this article.

Acknowledgments

This work was supported by the Science and Technology Project of Sichuan Province (2021YJ0354), the Zigong Key Science and Technology Project (2020YGJC02) and the Scientific Research and Innovation Team Program of Sichuan University of Science and Engineering (SUSE652A010).

References

Abramov, A., 2019. Optimization of well pad design and drilling–well clustering. Pet. Explor. Dev. 46 (3), 614–620. https://doi.org/10.1016/S1876-3804(19)60041-8.

Bahri, S.A., Musallami, A.A., Nicholas, G., 2024. Magnetic ranging technology for drilling operations. In: Abu Dhabi International Petroleum Exhibition and Conference. https://doi.org/10.2118/222270-ms.

Ben, J.L., Qiao, W.X., Che, X.H., et al., 2020. Field validation of imaging an adjacent borehole using scattered P-waves. Pet. Sci. 17 (5), 1272–1280. https://doi.org/10.1007/s12182-020-00475-5.

Cheng, L., Che, X.H., Qiao, W.X., et al., 2023. 3D trajectory inversion of an adjacent well using scattered P-wave. Pet. Sci. 20 (2), 857–865. https://doi.org/10.1016/j.petsci.2023.02.024.

Dorey, J., Rassadkin, G., 2021. Advancements in techniques for complex plug and abandonment using survey management and magnetic ranging methods. In: SPE Symposium: Decommissioning and Abandonment. https://doi.org/10.2118/208485-ms.

Dorey, J., Rassadkin, G., Ridgway, D., 2021. Complex subsurface well abandonments using relief well methodologies. In: SPE Annual Technical Conference and Exhibition. https://doi.org/10.2118/206311-MS.

Dou, X.Y., Liang, H.Q., Liu, Y., 2018. Anticollision method of active magnetic guidance ranging for cluster wells. Math. Probl Eng. 2018, 7583425. https://doi.org/10.1155/2018/7583425.

Dou, X.Y., Yan, X.P., Hu, L.Y., et al., 2024. Simulation research on the dual-electrode current excitation method for distance measurements while drilling. Appl. Sci. 14 (20), 9584. https://doi.org/10.3390/app14209584.

Dou, Z.J., Liu, Y.S., Qin, X., et al., 2022. Multi-objective optimization design of deviation-correction trajectory considering the production loss in shale gas cluster well. Pet. Sci. 19 (6), 2995–3003. https://doi.org/10.1016/j.petsci.2022.09.024.

Duncan, L.J., 2013. MWD ranging-A hit and a miss. Oil Gas Eur. Mag. 39 (1), 24–26.

Eatough, O., Alahmad, M., Momot, F., et al., 2018. Advanced well positioning with magnetic interference based on passive magnetic MWD ranging: case study. In: SPE Russian Petroleum Technology Conference. https://doi.org/10.2118/191502-18RPTC-MS.

ElGizawy, M., Fraser, M., Lowdon, R., et al., 2022. A novel realtime well collision avoidance monitoring by definitive dynamic surveys and passive magnetic ranging. In: Abu Dhabi International Petroleum Exhibition and Conference. https://doi.org/10.2118/211791-ms.

ElGizawy, M., Rakhmangulov, R., Allen, W., et al., 2024. Managing well collision risk by disruptive ranging technology without impacting rig time. In: SPE Annual Technical Conference and Exhibition. https://doi.org/10.2118/220770-MS.

Gao, D.L., Diao, B.B., Wu, Z.Y., et al., 2013. Research into magnetic guidance technology for directional drilling in SAGD horizontal wells. Pet. Sci. 10 (4), 500–506. https://doi.org/10.1007/s12182-013-0301-6.

Gao, D.L., Diao, B.B., 2016. Development of the magnetic guidance drilling technique in complex well engineering. Pet. Drill. Tech. 44 (5), 1–9. https://doi.org/10.11911/syztjs.201605001 (in Chinese).

Hao, P., Zhao, Y.P., Sun, X.Y., et al., 2021. Numerical investigation of active magnetic ranging method for relief well projects. In: 2021 IEEE International Geoscience and Remote Sensing Symposium IGARSS. IEEE, pp. 3514–3517. https://doi.org/10.1109/IGARSS47720.2021.9554757.

Hu, D.G., Liu, X.W., Diao, B.B., et al., 2021. Influence of axial magnetic interference on wellbore position uncertainty. In: IOP Conference Series: Earth and Environmental Science. IOP Publishing, 042004. https://doi.org/10.1088/1755-1315/651/4/042004.

Hu, Y.M., Yu, X.D., Weng, G.C., 2022. Magnetic steering drilling technology and its application in re-entry of borehole. Nat. Gas Explor. Dev. 45 (3), 57–66. https://doi.org/10.12055/gaskk.issn.1673-3177.2022.03.007 (in Chinese).

Hu, Z.Z., Fu, S.J., 2023. A method for ranging and positioning casing with high-intensity magnets: simulations and experimental studies. SPE J. 28 (5), 2116–2129. https://doi.org/10.2118/214676-PA.

Hu, Z.Z., Hou, Y., Li, Z.J., et al., 2019. Calculation and analysis of key parameter critical values in anti-collision design for upper sections of dense cluster wells. Oil Drill. Prod. Tech. 41 (4), 448–454. https://doi.org/10.13639/j.odpt.2019.04.008 (in Chinese).

Hu, Z.Z., Rao, X., Zeng, Y., et al., 2025. Computational method for determining subterranean pipeline direction using low-frequency current-generated magnetic fields. J. Pipeline Syst. Eng. Pract. 16 (4), 04025055. https://doi.org/10.1061/JPSEA2.PSENG-1582.

Hu, Z.Z., Ren, T.S., Fu, S.J., 2023. Research on anti-collision ranging method and key influencing factors of high intensity magnet. Pet. Sci. Technol. 41 (7), 761–782. https://doi.org/10.1080/10916466.2022.2090959.

Jackson, J.D., 2021. Classical Electrodynamics. John Wiley & Sons.

Jones, D.L., Hoehn, G.L., Kuckes, A.F., 1987. Improved magnetic model for determination of range and direction to a blowout well. SPE Drill. Eng. 2 (4), 316–322. https://doi.org/10.2118/14388-PA.

Li, C., Gao, D.L., Liu, Q.L., et al., 2016. A method of calculating of avoiding collisions with adjacent wells using electromagnetic ranging surveying while drilling tools. Pet. Drill. Tech. 44 (5), 52–59. https://doi.org/10.11911/syztjs.201605009 (in Chinese).

Li, F.L., Dang, B., Luo, X., et al., 2024. Modeling and simulation of electromagnetic ranging while drilling in relief wells. In: 2024 3rd International Conference on Energy and Electrical Power Systems (ICEEPS). IEEE, pp. 1080–1085. https://doi.org/10.1109/ICEEPS62542.2024.10693023.

Liang, H.Q., Geng, M., Shi, D.H., et al., 2013. A weak and frequency-varying signal detection method for rotating magnet ranging system. J. China Univ. Pet. Ed. Nat. Sci. 37 (4), 83–87. https://doi.org/10.3969/j.issn.1673-5005.2013.04.012 (in Chinese).

Lips, J.P., Rassadkin, G., Dorey, J., 2020. Connecting wells in environmentally sensitive areas using magnetic ranging-while-drilling technology for enhanced hydrocarbon recovery. In: SPE Latin America and Caribbean Petroleum Engineering Conference. https://doi.org/10.2118/199127-MS.

Liu, G., Wang, G., Wang, K., et al., 2023. Research status and development trend of anti-collision technology for dense cluster wells. China Offshore Oil Gas 35 (2), 146–154. https://doi.org/10.11935/j.issn.1673-1506.2023.02.016 (in Chinese).

Liu, Y.W., Guan, Z.C., Shi, Y.C., Wei, W.Z., Wang, D.H., Xiao, L.M., 2013. Analysis and treatment on vertical section collision accidents occurred in cluster directional wells and its revelation. Oil Drill. Prod. Technol. 35 (3), 45–47. https://doi.org/10.3969/j.issn.1000-7393.2013.03.013 (in Chinese).

Liu, Z.X., Wei, M.H., Zhang, P., et al., 2020. Drilling localization and error analysis of radial horizontal jet drilling based on magnetic gradient tensor. Energies 13 (19), 4989. https://doi.org/10.3390/en13194989.

Mojahid, A., Ouai, D.E.L., Amraoui, K.E.L., et al., 2025. Lightweight CNN model for automatic detection and depth estimation of subsurface voids using GPR B-scan data. Nat. Hazards Res. 5 (2), 432–446. https://doi.org/10.1016/j.nhres.2025.02.001.

Poedjono, B., Akinniranye, G., Conran, G., et al., 2007. Minimizing the risk of well collisions in land and offshore drilling. SPE/IADC Middle East Drilling Technology Conference and Exhibition. https://doi.org/10.2118/108279-MS.

Poedjono, B., Phillips, W.J., Lombardo, G.J., 2009. Anti-collision risk management standard for well placement. In: SPE Health, Safety, Security, Environment, & Social Responsibility Conference-North America. https://doi.org/10.2118/121040-MS.

Qin, C.H., Wang, Y., Ji, X.B., et al., 2025. The electromagnetic field analytical solution analysis to downhole current injection ranging. Appl. Sci. 15 (7), 3741. https://doi.org/10.3390/app15073741.

Shi, Y., Zhang, J.F., You, X.R., et al., 2024. Transient electromagnetic inversion to image the shallow subsurface based on convolutional bidirectional long short-term memory neural networks. Geophys. J. Int. 239 (1), 173–191. https://doi.org/10.1093/gji/ggae253.

Torkildsen, T., Håvardstein, S.T., Weston, J., et al., 2008. Prediction of wellbore position accuracy when surveyed with gyroscopic tools. SPE Drill. Complet. 23 (1), 5–12. https://doi.org/10.2118/90408-PA.

Wang, B., Liu, H., Ding, K., et al., 2003. Preparation of high property Nd-Fe-B magnets by SC process. J. Funct. Mater. 34 (5), 520–521. https://doi.org/10.3321/j.issn:1001-9731.2003.05.014.

Williamson, H.S., 2000. Accuracy prediction for directional measurement while drilling. SPE Drill. Complet. 15 (4), 221–233. https://doi.org/10.2118/67616-PA.

Wu, P., Wei, M.H., 2020. Magnetization influence analysis of the casing and drill pipe in shale gas dual horizontal well rotating magnet ranging system drilling process. Energy Sci. Eng. 8 (9), 3186–3199. https://doi.org/10.1002/ese3.730.

Wu, Z.Y., Gao, D.L., Diao, B.B., 2015. An investigation of electromagnetic anti-collision real-time measurement for drilling cluster wells. J. Nat. Gas Sci. Eng. 23, 346–355. https://doi.org/10.1016/j.jngse.2015.02.016.

Yan, X.P., Liang, H.Q., Dou, X.Y., et al., 2022. An active magnetic ranging method for drilling cluster wells based on casing current excitation. J. Pet. Sci. Eng. 208, 109784. https://doi.org/10.1016/j.petrol.2021.109784.

Zhang, D.R., Shi, Y.C., Chu, Z., 2015. Distribution of magnetic fields around vertical casings in geomagnetic field. China Pet. Mach. 43 (3), 12–16. https://doi.org/10.16082/j.cnki.issn.1001-4578.2015.03.003 (in Chinese).

Zhang, S., Diao, B.B., Gao, D.L., 2020. Numerical simulation and sensitivity analysis of accurate ranging of adjacent wells while drilling. J. Pet. Sci. Eng. 195, 107536. https://doi.org/10.1016/j.petrol.2020.107536.

Zhang, S., Diao, B.B., Gao, D.L., 2023. Analytical model and numerical simulation of relief well adjacent distance considering multi-layer media. Geoenergy Sci. Eng. 231, 212377. https://doi.org/10.1016/j.geoen.2023.212377.

Zhao, W.X., Huang, L.L., 2006. Research on preparation of high performance Nd-Fe-sintered magnets. J. Guangdong Non-Ferr. Met. 16 (4), 271–274. https://doi.org/10.3969/j.issn.1673-9981.2006.04.011 (in Chinese).

Zong, Y.B., Zhang, J., Shi, X.F., Sun, F., 2011. A high-precision guidance method of wellbore trajectory based on the rotary magnetic dipole. Acta Pet. Sin. 32 (2), 335–339. https://doi.org/10.7623/syxb201102024 (in Chinese).